

Date: November 12, 2014

Localization of Gamma-Ray Bursts using the *Fermi* Gamma-Ray Burst Monitor

V. Connaughton^{*,1}, M. S. Briggs¹, A. Goldstein², C. A. Meegan³, W. S. Paciesas⁴, R. D. Preece⁵, C. A. Wilson-Hodge², M. H. Gibby⁶, J. Greiner⁷, D. Gruber⁸, P. Jenke³, R. M. Kippen⁹, V. Pelassa³, S. Xiong³, H.-F. Yu^{7,10}, P. N. Bhat³, J. M. Burgess¹, D. Byrne¹¹, G. Fitzpatrick¹¹, S. Foley¹¹, M. M. Giles⁶, S. Guiriec¹², A. J. van der Horst¹³, A. von Kienlin⁷, S. McBreen¹¹, S. McGlynn¹¹, D. Tierney¹¹, & B.-B. Zhang³

ABSTRACT

The *Fermi* Gamma-ray Burst Monitor (GBM) has detected over 1400 Gamma-Ray Bursts (GRBs) since it began science operations in July, 2008. We

*Email: valerie@nasa.gov

¹CSPAR and Physics Dept, University of Alabama in Huntsville, 320 Sparkman Dr., Huntsville, AL 35899, USA

²Astrophysics Office, ZP12, NASA/Marshall Space Flight Center, Huntsville, AL 35812, USA

³CSPAR, University of Alabama in Huntsville, 320 Sparkman Dr., Huntsville, AL 35899, USA

⁴Universities Space Research Association, Huntsville, AL, USA

⁵Dept. of Space Science, University of Alabama in Huntsville, 320 Sparkman Dr., Huntsville, AL 35899, USA

⁶Jacobs Technology, Inc., Huntsville, AL, USA

⁷Max-Planck-Institut für extraterrestrische Physik, Giessenbachstrasse 1, 85748 Garching, Germany

⁸Planetarium Südtirol, Gummer 5, 39053 Karneid, Italy

⁹Los Alamos National Laboratory, NM 87545, USA

¹⁰Excellence Cluster Universe, Technische Universität München, Boltzmannstr. 2, 85748, Garching, Germany

¹¹School of Physics, University College Dublin, Belfield, Stillorgan Road, Dublin 4, Ireland

¹²NASA Goddard Space Flight Center, Greenbelt, MD 20771, USA

¹³Astronomical Institute, University of Amsterdam, Science Park 904, 1098 XH Amsterdam, The Netherlands

use a subset of over 300 GRBs localized by instruments such as *Swift*, the *Fermi* Large Area Telescope, INTEGRAL, and MAXI, or through triangulations from the InterPlanetary Network (IPN), to analyze the accuracy of GBM GRB localizations. We find that the reported statistical uncertainties on GBM localizations, which can be as small as 1° , underestimate the distance of the GBM positions to the true GRB locations and we attribute this to systematic uncertainties. The distribution of systematic uncertainties is well represented (68% confidence level) by a 3.7° Gaussian with a non-Gaussian tail that contains about 10% of GBM-detected GRBs and extends to approximately 14° . A more complex model suggests that there is a dependence of the systematic uncertainty on the position of the GRB in spacecraft coordinates, with GRBs in the quadrants on the Y-axis better localized than those on the X-axis.

Subject headings: gamma rays: bursts

1. Introduction

In four years of operation, the *Fermi* Gamma-ray Space Telescope has opened a new window to the world of Gamma-Ray Burst (GRB) spectroscopy. Observations by the Gamma-Ray Burst Monitor (GBM, Meegan et al. (2009)) between 8 keV and 40 MeV and the Large Area Telescope (LAT, Atwood et al. (2009)) from 20 MeV to hundreds of GeV have provided a high-energy view over an unprecedentedly broad energy baseline. Follow-up observations of LAT-detected GRBs have revealed the redshift of about a dozen GRBs detected above 100 MeV (Ackermann et al. (2013) and references therein; Ramírez et al. (2013); Levan et al. (2013); Leloudas et al. (2013); de Ugarte Postigo et al. (2013)). Determining the redshift of GRBs enables the study of the energetics and rest-frame properties of these events. Owing to the localization limitations of the GBM experiment, follow-up observations of GRBs localized at trigger time only by GBM were rare until we disseminated the results of the work presented here, in which uncertainties in GRB localizations are characterized. GRB 090902B (Abdo et al. 2009) was observed by ROTSE (Pandey et al. 2010) an hour after the trigger, with ROTSE tiling the GBM error circle hours before the burst was better localized using LAT and *Swift* data. A source was subsequently found in the ROTSE data at the position of the burst, providing the earliest measurements of the GRB afterglow. GRB 130702A was observed by the intermediate Palomar Transient Factory (iPTF), with the telescope tiling 72 square degrees in 10 separate pointings, and uncovering the afterglow of the GRB 4.2 hours after the GBM trigger (Singer et al. 2013). This was the first discovery of afterglow emission from observations that used only the GBM localization and did not require additional, more

accurate, positions from the LAT or from *Swift* to find the source in the large observed sky region. Since then, regular observations by iPTF of GRBs localized by GBM revealed the afterglows for eight more GRBs in 35 attempts (L. Singer et al., in preparation). In general, however, the small fields-of-view of the most sensitive follow-up telescopes have deterred regular observations of the degrees-scale uncertainty regions resulting from GBM localizations. A further discouraging aspect of GBM localizations is that the total error is often larger than the reported statistical uncertainty. Using a Bayesian method similar to that reported here, Briggs et al. (2009) analyzed 36 GBM GRB localizations and found the 68% confidence level systematic uncertainty to be $3.8 \pm 0.5^\circ$. Hurley et al. (2013) use a sample of 149 GRBs detected by GBM and by other instruments in the InterPlanetary Network (IPN) to infer a 90% confidence level systematic uncertainty of 6° . We report here a study of systematic uncertainties using over 300 reference locations provided by other instruments and by the IPN. The technique we use is based on the work of Graziani & Lamb (1996) and Briggs et al. (1999), who developed a Bayesian approach to characterize systematic uncertainties for the GRBs detected by the Burst And Transient Source Experiment (BATSE) on the Compton Gamma-Ray Observatory.

GBM detects about 240 GRBs per year (Paciesas et al. 2012; von Kienlin et al. 2014), providing real-time locations for the follow-up community. Approximately 17% of *Fermi* GBM-detected GRBs are short in duration (von Kienlin et al. 2014). Unlike the short GRB population detected by *Swift*, which may contain weak collapsar events (Bromberg et al. 2013), it is likely that most GBM-detected short GRBs (SGRBs) are associated with the merger of compact binary systems. There are therefore 40 or so merger GRBs per year detected by GBM that could potentially be observed at other wavelengths. Mergers of compact binary systems are likely sources of gravitational waves (GW). No associations were found between 154 GRBs detected in 2009-2010 by various spacecraft, including GBM, and potential signals in the LIGO and Virgo GW experiments (Abadie et al. 2012). This was not unexpected given the detection horizon of about 20 Mpc for these experiments. Advanced configurations of both experiments will be deployed over the next few years, with horizons of 400 [1000] Mpc for NS-NS [NS-BH] mergers (Abadie et al. 2010). It is realistic to expect several joint detections of SGRBs by GBM and GW candidates by A-LIGO/Virgo per year (Connaughton et al. 2013). For the first years of A-LIGO/Virgo operation, localization uncertainties for GW candidates are estimated to be 1000 square degrees or more (Aasi et al. 2013), larger than the GBM uncertainty regions, consisting of annuli segments that may encompass non-contiguous sky regions. It is especially important to enable the optical community to observe SGRBs while the afterglow is still bright enough to be detected above the background in a large error box. For GBM-detected SGRBs, this may imply covering only a small part of the error box.

In Section 2 we describe the detection and localization of GRBs by GBM and in Section 3 their dissemination to the public over the GRB Coordinates Network. The sample of reference locations from detections by other instruments or by the InterPlanetary Network is introduced in Section 4, where reference point locations are compared to the GBM localizations and their reported statistical uncertainties. In section 5, we describe our method to assess the effect of systematic uncertainties on GRB localization. We report results for the models we tested. In section 6 we summarize our results and describe new data products that use these results to facilitate follow-up observations of GRBs localized by GBM.

2. Localization of GRBs by GBM

The GBM views the entire unocculted sky, over 7 steradians, using 12 sodium iodide (NaI) detectors, 1.27 cm thick and 12.7 cm in diameter, covering an energy range from 8 keV to 1 MeV, and two bismuth germanate (BGO) scintillators, 12.7 cm in diameter and thickness, placed on opposite sides of the spacecraft, with energy coverage from 200 keV to 40 MeV (Meegan et al. 2009). In a coordinate system centered on the spacecraft, the Z-axis is oriented along the boresight of the LAT, the X-axis joins the two BGO detectors, and the Y-axis joins the LAT radiators, as shown in Figure 1. The placement of the NaI detectors, which all have different orientations, in four clusters of three detectors gives maximum coverage along the positive Z-axis. This means GRBs in the LAT field-of-view are seen by more GBM detectors than those outside. If *Fermi* were pointed at the local zenith, the Earth would occupy the region in spacecraft coordinates viewed by the fewest detectors, along the negative Z-axis. In nominal sky-survey mode, *Fermi* views the whole sky every 3 hours (2 spacecraft orbits) by tilting alternately north and south of the zenith each orbit to obtain uniform sky survey coverage when the exposure is averaged over just a few orbits. The angle of the tilt, called the rocking angle, has changed from 35° at the start of the *Fermi* mission to 50° in October 2009, the change being necessary to place *Fermi* in a rocking profile that keeps the spacecraft battery cool.

The energy information from the GBM detectors is binned in 128 channels constructed using the 4096 channels in the Data Processing Unit that result from the digitization of the analog output from the detector front-end electronics. Channel-to-energy conversion uses pre-launch exposures to radioactive sources between 14 keV and 4.4 MeV and a spline fit between and beyond the energies of the known sources covers the whole energy range. Details of the energy calibration are given in Bissaldi et al. (2009). The localization of sources is done with an 8-channel rebinning of the full-resolution 128-channel data into a quicklook data type that is downloaded in real-time when a trigger occurs.

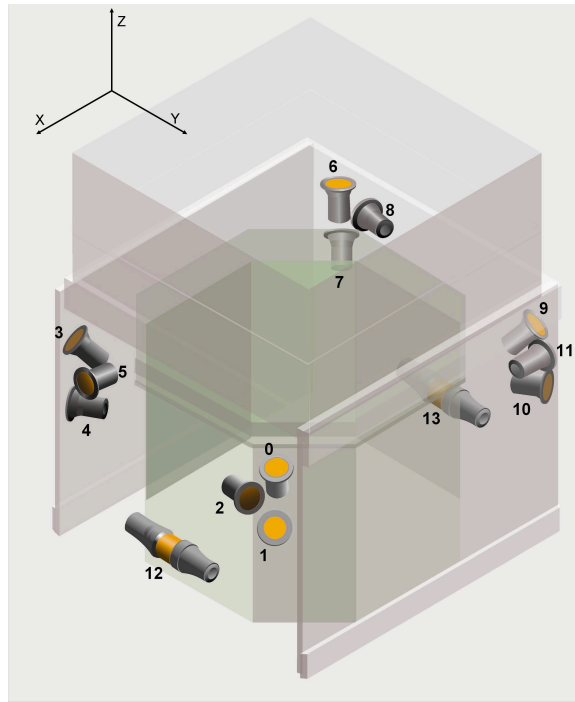


Fig. 1.— In the spacecraft coordinate system, the Z-axis is aligned with the LAT pointing. The 14 NaI detectors and 2 BGO detectors are mounted on the +ve and -ve X-axes. The NaI detectors are numbered 0-11 and the BGO detectors 0 and 1. The solar panels and LAT radiators are mounted on the +ve and -ve Y-axes.

Source localization uses the relative rates recorded in the 12 NaI detectors to estimate the most likely arrival direction given the angular and spectral response of the detectors. The detector response model was constructed from simulations incorporating the *Fermi* spacecraft mass model into GEANT4 (Kippen et al. 2007). Incident photons with energies between 5 keV and ~ 50 MeV were injected from 272 directions in the spacecraft coordinate system to evaluate the geometry-dependent detector response.

A χ^2 minimization process finds the direction on the sky from which the expected count rates from our detector response model most closely match the observed detector count rates in all 12 NaI detectors. The observed counts include a background component that is subtracted before modeling the source. The observed source counts are compared to expectation from evenly distributed points on a 1° resolution grid in spacecraft coordinates that linearly interpolates among the three closest of the native 272 sky directions giving 41168 grid points. The source rates contain three elements: direct flux from the source, flux scattered in the spacecraft, and flux scattered from the atmosphere. Contributions from each of these components depend on the observing geometry and on the spectrum of gamma rays from the source. We construct our instrument response matrices for a particular GRB by adding two model terms, the direct response, which depends only on the source-spacecraft geometry, and the atmospheric response, which depends on the source-spacecraft-Earth geometry. The direct response is calculated by interpolating among the three closest of 272 sky points in the native database compiled from the GEANT simulations. Our atmospheric response calculation is a simplification of the true geometry in which the Earth-spacecraft geometry has many solutions. We use the atmospheric response database established for BATSE (Pendleton et al. 1999). For each of the 41168 grid points we calculate the rates normal to each detector for the Earth-spacecraft geometry at the time of a trigger.

We construct three tables with the model count rates between 50 and 300 keV for each detector at each point on this grid, using three source spectra representing spectrally soft, medium, and hard GRBs. The source spectra are modeled using the Band function parametrization (Band et al. 1993), two power-law components, α and β , that are smoothly joined, and a peak in the power per decade of energy, E_{peak} :

$$F(E) = \begin{cases} \left(\frac{E}{100}\right)^\alpha \exp\left[-\frac{(\alpha+2)E}{E_{peak}}\right] & E < [(\alpha - \beta)E_{peak}]/(\alpha + 2) \\ = \left(\frac{E}{100}\right)^\beta \exp(\beta - \alpha) \left[\frac{(\alpha-\beta)E_{peak}}{100(\alpha+2)}\right]^{\alpha-\beta} & E \geq [(\alpha - \beta)E_{peak}]/(\alpha + 2) \end{cases}$$

The Band function parameters for these three spectra are α , β , $E_{peak} = (-1.9, -3.7, 70$ keV), $(-1, -2.3, 230$ keV), and $(0, -1.5, 1$ MeV). Thus, the direct response is fixed and depends only on the source position in spacecraft coordinates. To this we add an atmospheric

component that is calculated during the execution of the localization code and that depends on the position of the Earth in spacecraft coordinates. A χ^2 minimization of each of the three tables (soft, medium, hard) relative to the observed rates produces the most likely arrival direction in spacecraft coordinates for each of the three model spectra, and the lowest χ^2 among the three minima is assumed to be from the spectrum that most closely resembles the burst. The position from the selected table is translated to equatorial coordinates using the spacecraft attitude at trigger time. The reported 68% statistical uncertainty is the average distance to the grid points that lie at $\Delta\chi^2 = 2.3$, assuming a circular uncertainty region. A lower limit to the reported statistical uncertainty of 1° is imposed to match the grid resolution, though in practice the χ^2 contours can be very steep within the grid points. A discussion of the χ^2 distributions and the selection of the best model based on χ^2 is given in Appendix A.

3. GBM Localization types

It is desirable to generate GRB localizations as soon as possible after the trigger. An automated process requiring no human intervention produces initial localizations from the on-board Flight Software algorithms (FSW locations) and on the ground (Ground-Auto locations), both within 10-30 s of the GRB trigger. Refined ground locations use more data and human judgment (Human in the Loop, or HitL locations) and are distributed on the order of an hour later.

When a GBM trigger occurs on-board *Fermi*, the GBM flight software (FSW) produces trigger data types that are downlinked to the ground upon summoning the Tracking and Data Relay Satellite System (TDRSS) link, a 5 second process. In addition to activating a TDRSS link, the GBM FSW communicates with the LAT via the spacecraft bus, informing the LAT FSW that a trigger has occurred, its nature (GRB, solar flare etc.), and sends a localization produced by the FSW. Because of memory limitations on-board, the FSW localization uses a coarser sky grid than previously described (5°) and only one spectral model table, the Band function medium spectrum defined above, to which is added a pre-computed atmospheric scattering component that assumes the Earth is at the spacecraft nadir rather than calculating the atmospheric scattering component at trigger time. The first localization is produced by the FSW using the counts recorded in the most significant data accumulation on 17 time-scales ranging from 16 ms to 4.096 s, using data in the time interval leading to the trigger and an additional 1.5 s of data accumulated following the trigger time, to find a χ^2 minimum in the on-board model rates table. The LAT uses this location as a seed to allow a less stringent on-board trigger level than its usual all-sky on-

board science algorithm. The FSW produces further localizations if later data accumulations on time-scales from 16 ms to 4.096 s are more significant relative to the background level than the initial accumulation at 1.5 s post-trigger, with these later localizations communicated both to the LAT and to the ground.

In addition to the localizations produced by the FSW, TDRSS is also used to transmit the most significant count rates above background on the 16 ms to 4.096 s accumulation intervals, called MAXRATES, with MAXRATES transmission occurring only if the rates are more significant relative to the background level than previous MAXRATES calculations on any time-scale. Finally, a background count-rate record is transmitted that contains the average count rates in each detector over a 16 s period prior to the trigger time and separated from the trigger window by 3 s. After reception on the ground, MAXRATES and background packets, which also contain spacecraft position and attitude information, are ingested into the Burst Alert Processor (BAP) at NASA GSFC (or its backup at the GBM Instrument Operations Center in Huntsville). The FSW-determined background rates are subtracted from the MAXRATES to give source rates that are compared to the models. A Ground-Auto localization is generated using the full-resolution model rates tables including an atmospheric response component that uses the true Earth position rather than assuming a zenith-pointed *Fermi* spacecraft. Both FSW and Ground-Auto localizations are communicated as notices to the GRB Coordinates Network (GCN) if the statistical uncertainty is lower than previous FSW or Ground-Auto notices.

Over the next ten minutes, the FSW transmits via TDRSS a count rate time history covering from 200 s prior to 450 s following the trigger time, and the BAP alerts the GBM Burst Advocate (BA) to the presence of a trigger so that a HitL location can be generated when the real-time data set is complete. Both the FSW and the Ground-Auto locations use single accumulations in intervals from 16 ms to 4.096 s and can thus be considered peak-flux localizations. For the HitL localizations, the BA can select a source interval to produce a fluence localization that should in many cases yield a localization with a smaller statistical uncertainty. The BA selects time intervals before and after the burst emission to fit with a polynomial of order up to 4 as a background model that is subtracted from the observed counts in the source interval prior to the χ^2 minimization.

The three types of localizations are distributed without delay via GCN notices using email and socket connections. FSW notices are sent out for all triggers and include a trigger classification (see Meegan et al. (2009) for a discussion of the FSW trigger classification procedure). Ground-Auto notices are distributed only if the FSW classified the trigger as a GRB at the time the MAXRATES packet was produced and the Ground-Auto localization passed an automated χ^2 quality test (i.e., the localization appears consistent with a distant

point source based on the relative rates in the detectors). HitL positions are sent as Final Position notices only if the BA classifies the event as a GRB and the GRB has not been localized more precisely by another instrument at the time of the HitL processing. Table 1 summarizes the types of locations, their reported statistical uncertainties, the typical latencies until the first GCN notice is issued, and the number of notices of each type issued for a trigger classified by the FSW as a GRB.

Latencies for the FSW notices have been stable since launch. An update to the ground localization software in 2011 resulted in longer latencies for the Ground-Auto notices owing to limitations of the BAP hardware and the processing in parallel of multiple MAXRATES packages. An upgrade of the BAP hardware occurred in 2012 and the BAP processing software was also modified to reduce latencies and send notices only if the reported localization uncertainty is smaller than previous notices for that trigger. These changes have resulted in fewer, but more useful, Ground-Auto notices that are distributed more quickly. In 2011, the BAs began distributing the HitL position as a GBM notice, with latencies depending on data availability and BA response time.

4. Comparison of GBM localizations with known GRB locations

Between July 2008 and May 2013, GBM triggered on 203 GRBs that were well-localized by other instruments or by the IPN, with location uncertainties (68 % confidence level) smaller than 1° . These 203 reference locations are listed in Appendix B, Table 9. The ground localization software has been changed several times during the mission. The current version of the code is 4.14g, for both the HitL and the Ground-Auto localizations, and this version is used for comparing the GBM locations with the 203 reference locations, so that the positions are recalculated using the current version rather than using the GRB positions distributed via GCN notices and circulars. It should also be noted that the HitL localizations used in this analysis were redone to ensure the background model and source selection were uninfluenced by the known reference positions. On-board localization software has not changed since 2008 October 1 and the FSW locations are assessed using the 192 reference locations from GRBs that occurred after this date.

The main purpose of the FSW locations is to alert the LAT to the occurrence of a GRB. This allows the LAT FSW to adjust its on-board algorithm parameters using the temporal and spatial information from GBM. If the GRB is bright or spectrally hard enough, as determined by the GBM FSW, the FSW location is also used to place the GRB near the center of the LAT Field-of-View (FoV) following an Automatic Repoint Recommendation (ARR) issued by the GBM FSW to the spacecraft. Because the FoV of the LAT is $\sim 65^\circ$, the

requirements on the FSW localization are loose, 20° uncertainty (68% CL) with a goal of 15° . Figure 2 shows the fraction of FSW localizations within a given offset of the true location for the 192 reference locations. The top panel shows the quality of the initial location, calculated at 1.5 s post-trigger. This can be compared in the bottom panel with the final FSW locations sent out as a GCN notice, a set that includes the initial FSW localizations of GRBs for which only one FSW location was issued. The vertical lines show that 68% of the true positions are contained in a 14.9° [11.6°] region for the initial [final] FSW locations, with 90% contained within 31.9° [25.1°]. This is sufficiently accurate for the LAT and the ARR process, and perhaps useful for the follow-up observer on the ground as an alert to begin slewing the telescope a few seconds before the more accurate Ground-Auto locations become available.

Figure 3 shows the true offset from the known source position as a function of the reported statistical uncertainty for both HitL (top) and Ground-Auto (bottom) localizations. Where more than one possible Ground-Auto position exists, we use the last one produced by the BAP that would have been sent out as a notice. Figure 4 shows the fraction of GBM localizations within a given offset of the true location for HitL (top) and Ground-Auto locations. The vertical lines show that 68% of the true positions are contained in a 5.3° [7.6°] region around the HitL [Ground-Auto] locations, with 90% contained within 10.1° [17.2°]. Although the Ground-Auto positions appear significantly poorer, it can be seen from Figure 5 that when the offset to the true position is expressed as a multiple of the statistical uncertainty (68% CL), the quality is similar. This reflects the fact that the Ground-Auto locations are peak flux calculations that have fewer source counts than the fluence HitL localizations, resulting in larger statistical uncertainties. The horizontal solid and dashed lines show the fraction of localizations within 1 and 2σ . If the statistical uncertainties reflected the total error, the 1σ circles should contain 68% of the true source positions but they actually contain 39% [38%] of the true source positions for the HitL and Ground-Auto locations, respectively, increasing to 70% [74%] for the 2σ regions. This indicates that there is, in addition to the statistical uncertainty, a systematic component to the localization error.

Figure 6 shows the fraction of precisely localized GRBs (statistical uncertainty equal to 1.0°) lying within a given distance of a known position for both HitL and Ground-Auto localizations.

These distributions can serve as a guide to the follow-up observer wishing to concentrate on the brightest, best-localized events without worrying too much about covering the whole uncertainty region, but wanting to know how often they will succeed as a function of how much sky they are willing to tile. A more effective search strategy requires knowledge of the systematic uncertainty in order to probe the larger sky regions that contain most of the

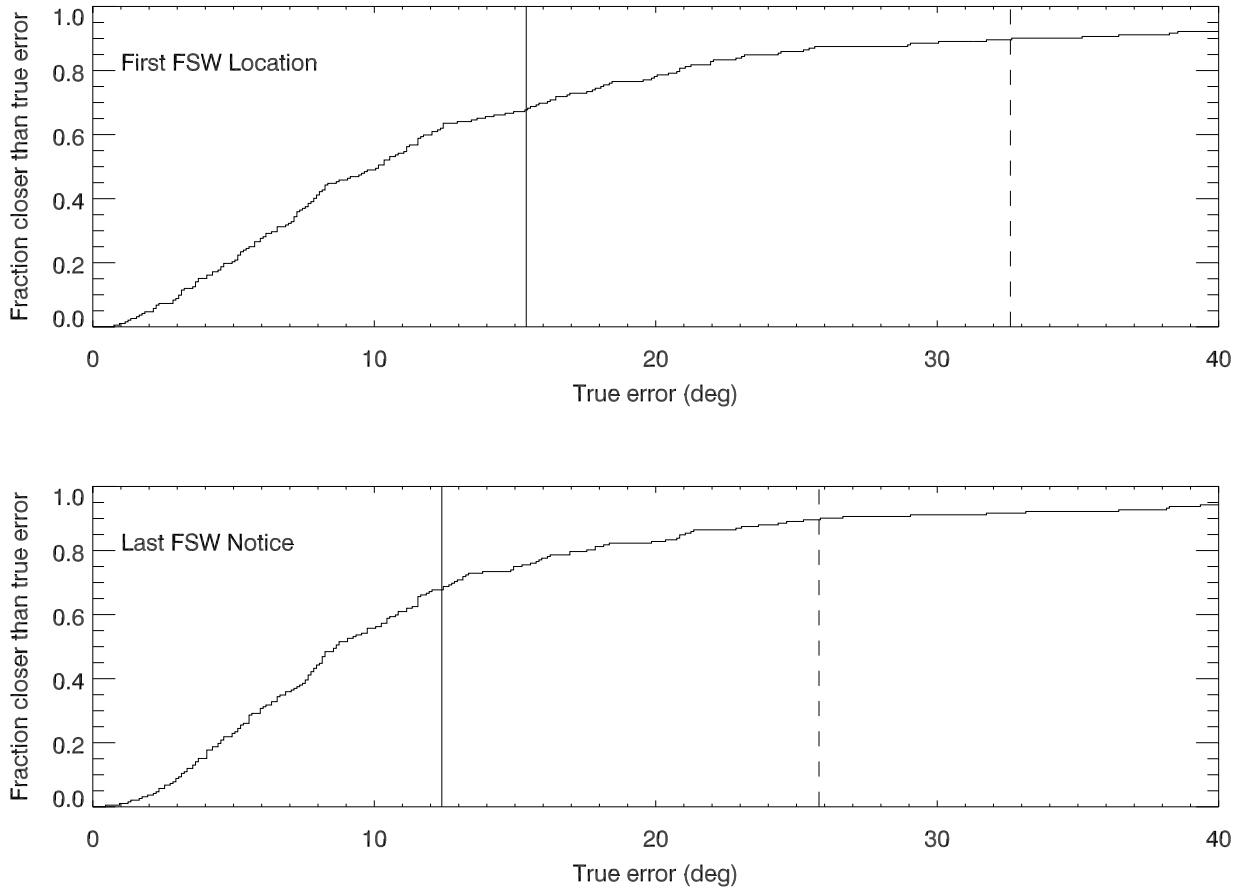


Fig. 2.— The histograms show the fraction of GBM FSW localizations lying within a given offset (degrees) from the true positions for the initial (top) and final (bottom) FSW locations. The solid vertical lines indicate the 68% containment radius of 14.9° and 11.6° , the dashed vertical lines the 90% containment radius of 31.9° and 25.1° .

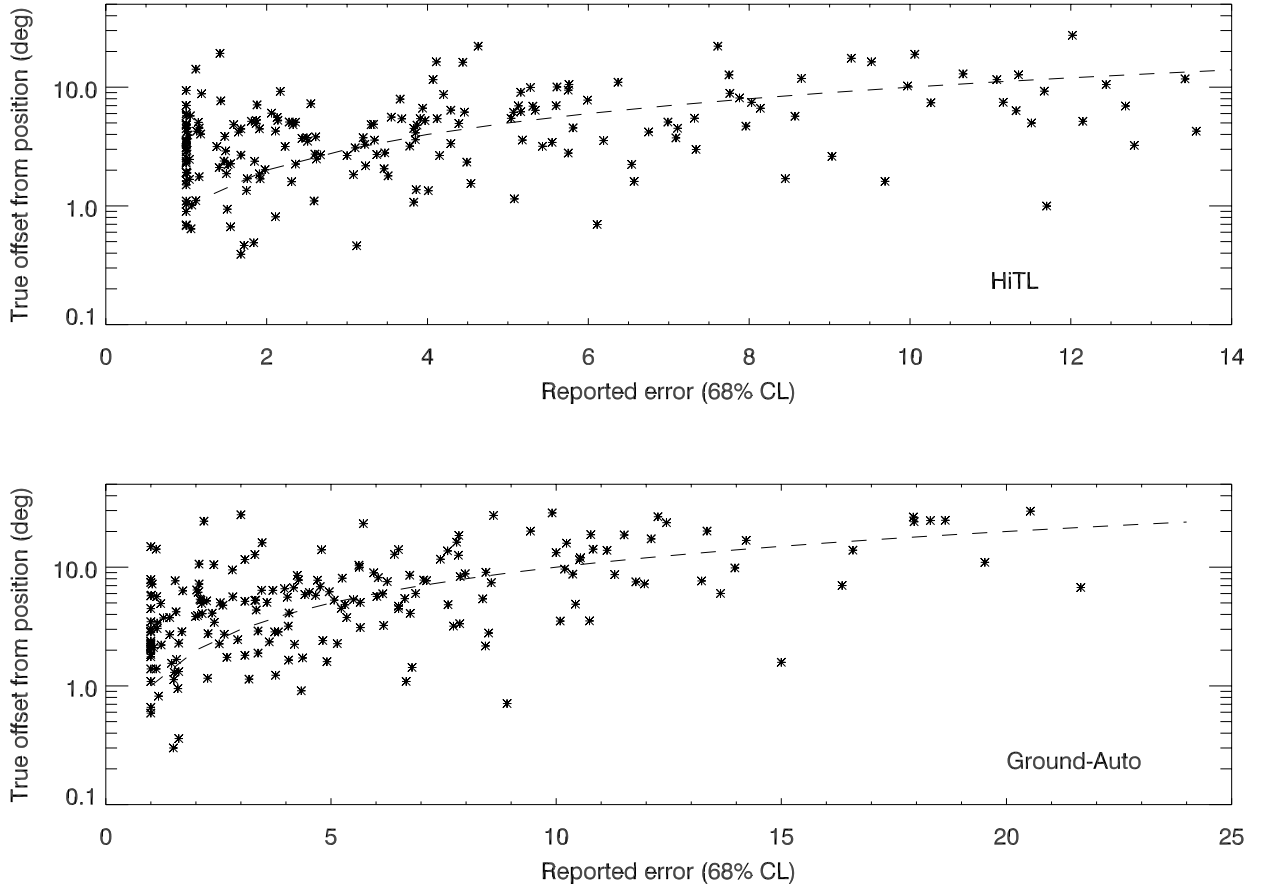


Fig. 3.— True offsets (degrees) from known positions for HitL (top) and Ground-automated (bottom) localizations as a function of the 68% CL statistical uncertainties in the localization. The dashed line shows equality between the quantities. A handful of Ground-Auto positions with uncertainties larger than 30° have been suppressed.

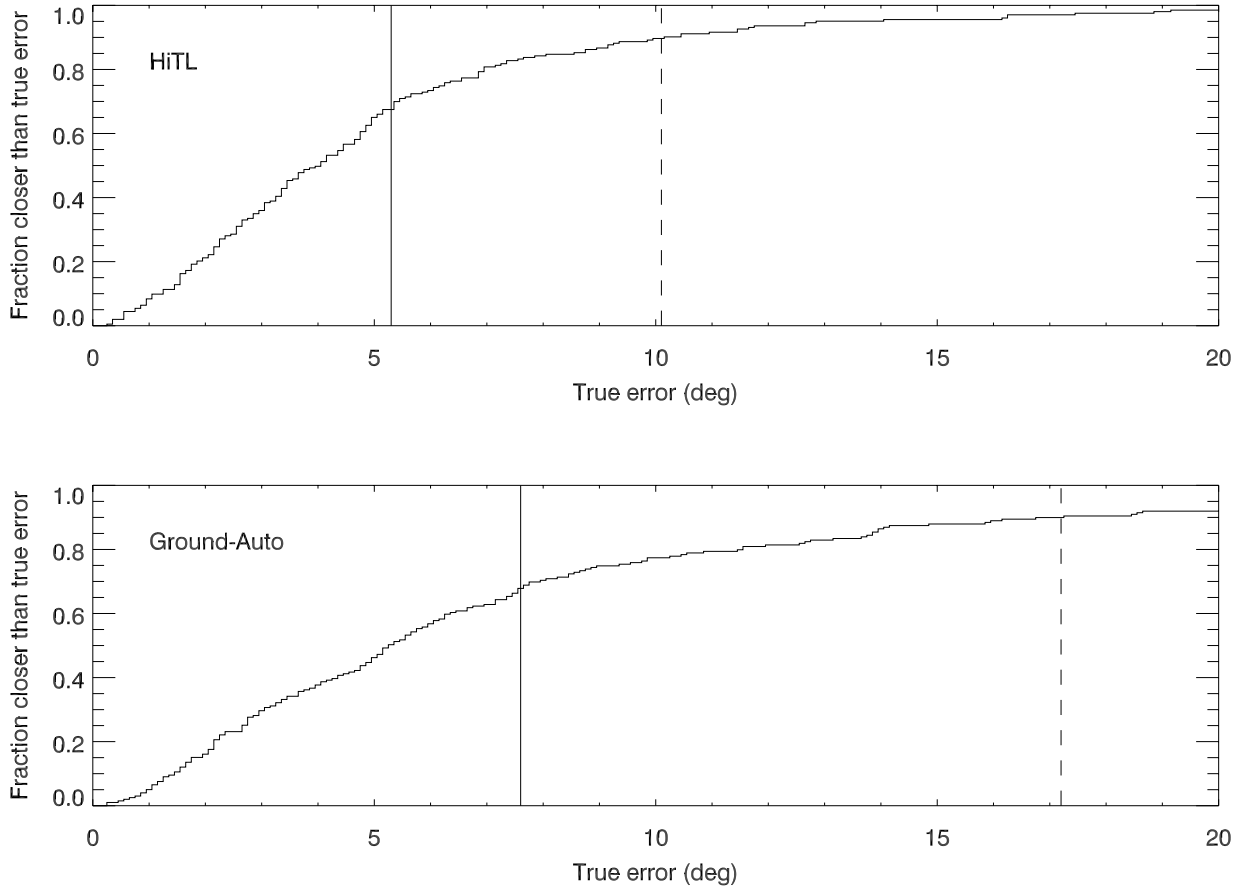


Fig. 4.— The histograms show the fraction of GBM localizations lying within a given offset (degrees) from the true positions for HiTL (top) and Ground-automated (bottom) positions. The solid vertical lines indicate a 68% containment radius of 5.3° [7.6°], the dashed vertical lines the 90% radius of 10.1° [17.2°].

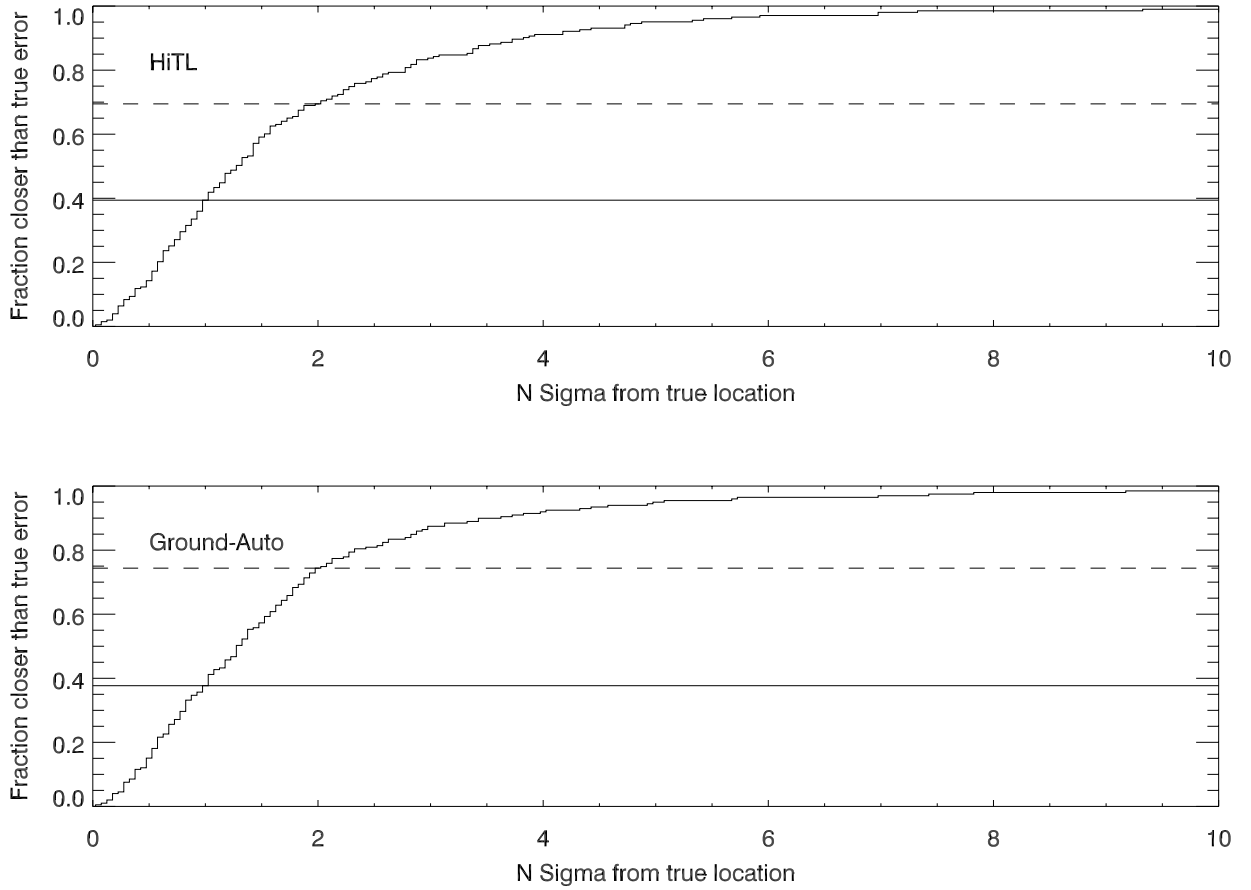


Fig. 5.— The histograms show the fraction of GBM localizations lying within a given offset from the true positions for HiTL (top) and Ground-automated (bottom) positions expressed as a multiple of the 68% statistical uncertainties. The solid horizontal lines indicate the reported 1σ containment radius actually encompasses about 40% of the events, with the dashed lines showing about 70% of events are contained within the 2σ region.

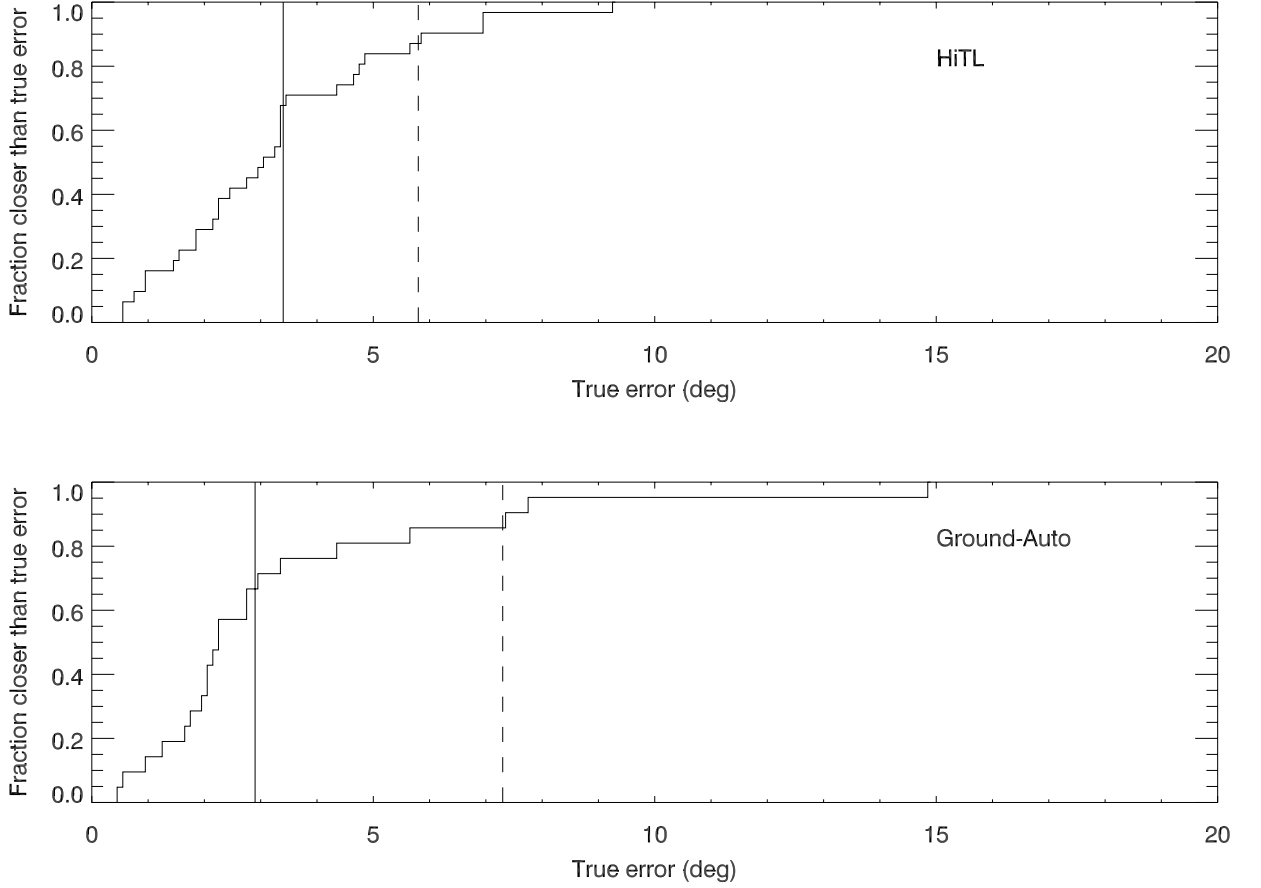


Fig. 6.— The histograms show the fraction of GBM localizations lying within a given offset (degrees) from the true positions for HitL (top) and Ground-automated (bottom) positions with statistical uncertainties of 1° . The solid vertical lines indicate the 68% containment radius (3.4° or 2.9°), the dashed vertical lines the 90% radius (5.8° or 7.3°). There are 31 GRBs in the HitL sample, 21 in the Ground-Auto sample. The 68% containment region for the 68% containment radius for the HiTL sample lies between 3.3° and 4.7° with the 90% containment radius having a lower limit of 4.7° and being unconstrained at the upper end. The 68% containment region for the 68% containment radius for the Ground-Auto sample lies between 2.2° and 5.6° with the 90% containment radius having a lower limit of 4.3° and being unconstrained at the upper end.

probability of the GRB arrival direction. This is of particular interest for archival searches by the multi-messenger community with instruments that do not require pointing a telescope to the source. The sensitivity of such searches, and of any upper limits obtained in the case of a null result, depends on defining a source region narrow enough to reduce the background but that is still wide enough to capture the source. In view of the connection between GRBs and core-collapse supernovae and the long time interval that can separate the events, it is also essential to define GRB directions in order to connect or reject GRB associations with observed SNe events, as was done, for example, by Soderberg et al. (2010) in the case of SN 2009bb. This will become increasingly important in the era of the Large Synoptic Survey Telescope (LSST) and the expected discovery of many more optical transients in search of counterparts at other wavelengths.

In the following section, we characterize the systematic uncertainty associated with GBM localizations in order to be able to calculate the probability that any region contains the actual source location. We concentrate on the ground localizations that are most useful to devising a follow-up strategy although, for completeness, we will briefly characterize the systematic uncertainty associated with the FSW localizations. The reference sample includes the point source locations discussed above and annuli obtained through triangulation by the IPN. For analysis convenience we use only reference locations that may be considered to be points and annuli that may be considered to be lines, with respect to the GBM localization. We include IPN annuli with 3σ half-widths narrower than 0.8° . For some GRBs the IPN has multiple arcs that intersect to provide an accurate location, with an intersecting region that has a corner-to-corner dimension of less than 1.6° ; in these cases we use the intersection closest to the GBM location as a point location. When the IPN has multiple arcs that do not provide an accurate location we use only the narrowest arc in order not to overweight that GRB in the sample. In addition to the 203 point locations described above, 134 GRBs from the IPN - GBM catalog (Hurley et al. 2013) between July 2008 and July 2010 provided 244 annuli, shown in Appendix B, Table 10. After removing annuli that were wider than 1.6° and collapsing intersecting annuli to point sources, this IPN catalog supplied 100 annuli and 9 additional point sources (from 18 intersecting annuli). The 1.6° acceptance limit for the IPN annuli ensures that only annuli with dimensions smaller than the smallest GBM localization uncertainty are used in the reference sample. Wider annuli would not influence the model fits because their contribution to the constraints on the model parameters would be weighted by the large uncertainty in the dimension (width) that is used to evaluate the best-fit parameters and the goodness-of-fit of the model, but the reference sample would appear larger than the true useful reference sample. These criteria then provide a reference sample with $N_{\text{point}} = 212$ point locations and $N_{\text{arc}} = 100$ arcs.

In Figure 7, we compare the properties of our reference sample to the population of

GRBs detected over the same period of time. Although the GRBs in our reference sample are, on average, brighter than other GRBs detected by GBM, with more source counts leading to smaller statistical localization errors, they are more representative of the overall population of GRBs detected by GBM than the reference sample in Briggs et al. (1999) is of the overall GRB population detected by BATSE. The reference GRB population in this work is drawn from experiments with higher fluence thresholds (IPN, *Fermi*-LAT) but also from experiments with equal or lower fluence sensitivity (*Swift*-BAT, INTEGRAL), whereas the reference sample in Briggs et al. (1999) comprised only GRBs bright enough for detection by the IPN.

5. Investigating the systematic uncertainty associated with GBM localizations

We use a Bayesian approach to find a model characterizing the systematic uncertainties in GBM localizations. This approach was used by Briggs et al. (1999) to show that the systematic uncertainties in BATSE GRB localizations were better fit using a model that contained most of the probability in a core distribution that peaked at 1.6° , with a larger uncertainty in an extended tail, than by a single component.

The GBM localization program estimates a statistical location uncertainty, σ_{stat} . The localization errors are larger due to systematic errors, so we represent the total location uncertainty as $\sigma_{\text{tot}}^2 = \sigma_{\text{stat}}^2 + \sigma_{\text{sys}}^2$. The errors are assumed to be azimuthally symmetric. The models are based on the Fisher probability density function, which has been called the Gaussian distribution on the sphere (Fisher et al. 1987):

$$p_{\text{F}}(\gamma) d\Omega = \frac{\kappa}{2\pi(e^\kappa - e^{-\kappa})} e^{\kappa \cos \gamma} d\Omega, \quad (1)$$

where γ is the angle between the measured and true location, κ is termed the concentration parameter and $d\Omega$ is solid angle. Considering σ_{tot} to be the radius of the circle containing 68% of the total probability, integrating eq. 1 relates κ and σ_{tot} in *radians* (Briggs et al. 1999):

$$\kappa = \frac{1}{(0.66\sigma_{\text{tot}})^2}. \quad (2)$$

We find equation 2 works well over a broad range of σ_{tot} and use it for all values in our sample.

For comparison with point reference locations, we denote the separation between a GBM localization and the reference location as γ , while for an arc we denote the separation between the GBM localization and the closest point on the center-line of the annulus as ρ . Of course, the true separation might be larger than ρ . Our aim is to develop and test models for

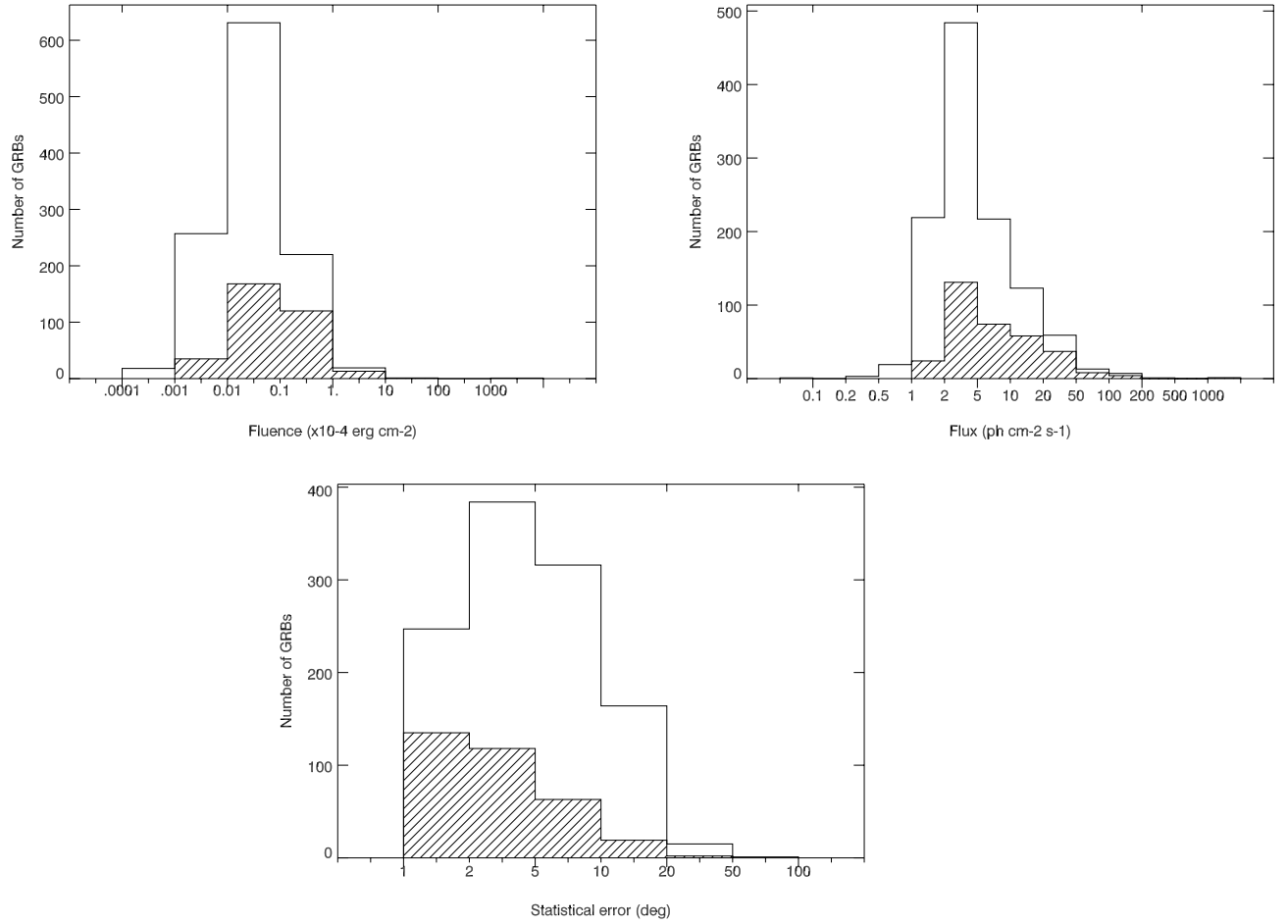


Fig. 7.— Comparison of the properties of GRBs in the reference sample (hashed) to those of the general population of GRBs detected by GBM (solid). The panels show (a) fluence (b) 1-s peak flux between 10 - 1000 keV (c) $1\text{-}\sigma$ statistical uncertainty on the HitL localization.

the GBM localization probability density function $p_\gamma(\gamma)$. We assume the GBM localization probability $p_\gamma(\gamma)$ is a Fisher function or the sum of two Fisher functions:

$$p = fp_F(\gamma_1) + (1 - f)p_F(\gamma_2). \quad (3)$$

For these cases, the probability density function $p_\rho(\rho)$ is known analytically (Briggs et al. 1999).

We use Bayesian model comparison to test models for the systematic error (Loredo 1990; Sivia 1996). Bayesian model comparison is based on the likelihood, which is the product of the probabilities of the observed offsets:

$$\mathcal{L} = \prod_i p_\gamma(\gamma_i) \prod_j p_\rho(\rho_j). \quad (4)$$

The equation shows the dependence of the likelihood \mathcal{L} on the offsets γ_i , $i = 1, \dots, N_{\text{point}}$ and ρ_j , $j = 1, \dots, N_{\text{arc}}$; \mathcal{L} also depends on the error model and is a function of the error model parameters through the functions p_γ and p_ρ . The reference data are of two types, point locations and arcs, disparately testing the quality of the GBM localizations. The Bayesian model comparison naturally handles the difference in evidence since both types of reference data are included in the likelihood via probabilities.

A complicated model with many parameters may have improved likelihood because the model is better or because the additional parameters allow the model to conform to statistical fluctuations. The question is, is the improvement in likelihood sufficient that we should believe in the more complicated model? Bayesian model comparison handles this problem by penalizing models with additional parameters with Occam's factors F . Assuming that a reasonable range, or prior, for the parameter λ_k is from λ_k^{\min} to λ_k^{\max} , that the model fitting has estimated the parameter uncertainty as σ_{λ_k} and that the likelihood function is approximately Gaussian, the Occam's factor for parameter λ_k is (Sivia 1996):

$$F_k = \frac{\sigma_{\lambda_k} \sqrt{2\pi}}{\lambda_k^{\max} - \lambda_k^{\min}}. \quad (5)$$

We consider all of the models equally plausible (i.e., identical priors), so that the Odds ratio $O_{B/A}$ by which one should favor model B over model A is

$$O_{B/A} = \frac{P(B)}{P(A)} = \frac{\mathcal{L}(B) \times \prod F_b^B}{\mathcal{L}(A) \times \prod F_a^A}. \quad (6)$$

Instead of listing the Odds ratios $O_{B/A}$ for every combination of models A and B we calculate in Tables 2 to 8 the quantities

$$\log_{10}[\mathcal{L}(M) \times \prod F_k^M]. \quad (7)$$

The base-10 logarithm of the Odds factor of two models may be obtained by differencing these values.

The following models were tested (where we use the term Gaussian to denote the Fisher function):

- A single component fit by a Gaussian. This model has a single parameter, the peak position of the Gaussian.
- A single component modeled by a Gaussian, split into 2 populations depending on the hemisphere containing the GRB position, in spacecraft coordinates. One model each for the X, Y and Z hemispheres splits the GRBs into positive and negative hemispheres. These models have two parameters: the peak of the Gaussian for bursts in each hemisphere.
- To explore the effects of the symmetry of the *Fermi* spacecraft on the GBM localization accuracy, the samples were also divided according to quadrant, with GRB positions within the $\pm X$ quadrants separated from those localized within the $\pm Y$ quadrants. These models have two parameters: the peak of the Gaussian for bursts in each quadrant set.
- A core-plus-tail modeled by two Gaussians. This model has three parameters: the peak position of each Gaussian and the fraction in the core.
- A core-plus-tail modeled by two Gaussians, split into 2 populations depending on the hemisphere of the GRB position, in spacecraft coordinates (one model each for the X, Y, and Z hemispheres). Each model has six parameters: the peaks of the two Gaussians and the fraction in the core, for each hemisphere.
- A core-plus-tail modeled by two Gaussians, split into two sets of quadrants, one containing the GRBs located within the $\pm X$ quadrants, the other within the $\pm Y$ quadrants. This model, like the hemisphere models, has six parameters.

Tables 2 and 3 show the results for the most basic single-component and core-plus-tail fits to the systematic uncertainties on the Ground-Auto, and HitL localizations. In addition to the current version of the localization software, 4.14g, fits for version 4.13 of the HitL localization are included in order to characterize the localizations in the first pair of GRB catalogs and part of the second pair of GRB catalogs (Paciesas et al. 2012; Goldstein et al. 2012; von Kienlin et al. 2014; Gruber et al. 2014), which used this older version. The main change implemented in 4.14g was the selection of a model spectrum based on the χ^2 values

Notice Type	Latency		Type	Error		Number
	Minimum	Typical		Minimum	Typical	
On-board (FSW)	4 s ¹	15-30 s	Peak Flux	3 °	8-15 °	1-3
Ground-Auto (GA)	12 s					
GA 2008-2010		30-60 s	Peak Flux	1 °	5 °	1-5
GA 2011-2012		60-150 s	Peak Flux	1 °	5 °	1-5
GA current		30-40 s	Peak Flux	1 °	5 °	1-3
Human-processed (HitL)	19 min	30-60 min	Fluence	1 °	3 °	0-1

Table 1: Types of localization produced by GBM for GRB triggers. Localization uncertainties are 68% CL statistical uncertainties. The Ground-Automated notice latency has varied throughout the mission as described in the text, and each configuration is listed separately. The Human-processed (HitL) notices are a new feature implemented in late 2011. ¹ This latency is lower than the time required to activate the TDRSS link, suggesting the link was already active at trigger time

Single-Component Gaussian						
Type	Number GRB Point	Annuli	Peak °	Error °	Log ₁₀ Likelihood	Log ₁₀ Odds Factor
Ground-Auto	208	100	6.62	0.29	155.2	154.3
HitL 4.14g	212	100	5.15	0.22	224.6	223.6
HitL 4.13	211	100	6.23	0.26	192.6	191.7

Table 2: Single-component fits to systematic uncertainties on GBM localizations of different types.

Core + Tail (2 Gaussians)										
Type	Number GRB Point	Annuli	Core °	Error °	Core %	Error %	Tail °	Error °	Log ₁₀ Likelihood	Log ₁₀ Odds Factor
Ground-Auto	208	100	3.72	0.34	80.4	5.3	13.7	1.7	174.1	171.8
HitL 4.14g	212	100	3.71	0.24	90.0	3.5	14.3	2.5	241.3	238.9
HitL 4.13	211	100	3.57	0.32	79.8	5.3	12.7	1.5	213.5	211.1

Table 3: Core-plus-tail fits to systematic uncertainties on GBM localizations of different types.

of the best-fit location using all three model spectra rather than *a priori* using three bands of hardness ratio values to classify the GRB as soft, medium, or hard and finding the χ^2 minimum only in the single corresponding model rates table. Looking at the difference between the odds factors between the single-component fits in Table 2 and the core-plus-tail fits in Table 3, it can be seen that a core-plus-tail model is favored over a single component model by factors of 10^{17} , 10^{16} , and 10^{19} for the Ground-Auto, HitL 4.14g, and HitL 4.13, respectively. The fraction in the core for the HitL localizations is higher using the more recent code, consistent with Version 4.14g being more robust, although the core values agree within errors, and are in fact slightly lower using the older code.

Results for single-component models exploring the effects of GRB location in spacecraft coordinates on the systematic error are shown in Appendix C. Table 11 shows that parameter values are similar for the systematic errors of GRBs in each of the hemispheres. There is no consistent statistical preference among the three localization types for models based on GRB position in spacecraft coordinates although individual localization types show slight preferences for hemisphere- or quadrant- dependent models. Owing to the placement of the GBM NaI detectors, which maximizes sensitivity in the +Z hemisphere to optimize coverage of GRBs in the LAT FoV, GRBs in the +Z hemisphere are more plentiful, viewed by more detectors, and might be expected to have more accurate localizations. The weak sensitivity of the systematic error to GRB position along the Z-axis suggests that any such effect is encompassed with a larger statistical error for the bursts viewed with fewer detectors in the -Z hemisphere. If we look at the cumulative fraction of GRBs lying within a given offset of the true location, we find that for HitL 4.14g the 68% [90%] containment radius is 5.1° [9.9°] for GRBs localized in the +Z hemisphere versus 5.3° [10.9°] for those in the -Z hemisphere. This difference is larger for version 4.13: 6.1° [11.1°] in the +Z hemisphere versus 6.8° [15.0°] in the -Z hemisphere, consistent with the results shown in Table 11. These numbers also suggest the overall quality of the 4.14g locations is higher than the older version and fewer outliers are produced. The odds ratios for all of the single-component models are much lower than the core-plus-tail model in Table 3, which is thus greatly preferred over any of the single-component models.

Results for core-plus-tail models that explore the effect of GRB position in different spacecraft hemispheres are described in Appendix D. Table 12 shows that localizations using HitL 4.14g are fit with lower parameter values for GRBs in the +Z hemisphere, although this model is not preferred statistically over the simpler, all-sky core-plus-tail model in Table 3. Other hemisphere-dependent core-plus-tail models did not yield significantly different parameters in the two hemispheres, nor were they statistically favored.

Table 4 shows the model fit parameters for localizations grouped according to GRB

Core + Tail (2 Gaussians) with quadrant dependence											
Type	Quadrants	Number GRB Point	Annuli	Core °	Error °	Core %	Error %	Tail °	Error °	Log ₁₀ Likelihood	Log ₁₀ Odds Factor
Ground-Auto	All-sky	208	100	3.72	0.34	80.4	5.3	13.7	1.7	174.1	171.8
Ground-Auto	± X	208	100	4.10	0.48	75.4	8.2	13.1	2.1		
	± Y			3.06	0.61	80.6	8.9	12.9	2.9	175.0	171.7
HitL 4.14g	All-sky	212	100	3.71	0.24	90.0	3.5	14.3	2.5	241.3	238.9
HitL 4.14g	± X	212	100	4.30	0.38	90.3	5.9	15.0	4.8		
	± Y			3.34	0.26	92.0	3.5	14.5	3.5	242.6	238.7
HitL 4.13	All-sky	211	100	3.57	0.32	79.8	5.3	12.7	1.5	213.5	211.1
HitL 4.13	± X	211	100	4.22	0.87	72.8	15.5	11.5	2.4		
	± Y			3.24	0.35	89.4	5.1	16.8	3.3	216.2	213.0

Table 4: Quadrant-dependent core-plus-tail fits to systematic uncertainties on GBM localizations.

position within the $\pm X$ and $\pm Y$ quadrants. Unlike the grouping into hemispheres, the differences in parameter values for quadrant-dependent models for all three types of localization cannot be explained by juggling events from the core to the tail. Instead, the $\pm Y$ quadrant GRBs are more likely to be localized with a systematic error in the core, and the value of the systematic error in the core is smaller than for events in the $\pm X$ quadrants. The odds factors for these models can be compared with the all-sky core-plus-tail model repeated in line 1 of the table. This 6-parameter model is favored only for HitL 4.13, which had a larger population of outliers in the tail than HitL 4.14, but the parameter values are suggestive that this 6-parameter model should be favored over the simpler 3-parameter core-plus-tail model with a larger sample or more judiciously chosen quadrants.

Table 5 displays the quadrant-dependent core-plus-tail model parameters and odds ratios with sliding quadrant azimuth ranges. A larger sample of reference locations will, in the future, allow the quadrant ranges to vary as free parameters but a model with these extra free parameters is too complicated to converge with the current sample. The core-plus-tail models are significantly preferred over single Gaussians so that optimizing the quadrant azimuth ranges with a single Gaussian model is not explored. Entry 1 is the standard all-sky core-plus-tail model, which was found to represent the data better than any of the single-component models we explored. Entry 2 has equal azimuth ranges in each quadrant. Entry 3 explores the effect of making the $\pm Y$ quadrant bigger. This provides no improvement and moves the quadrant core parameter values closer to each other. Narrowing the $\pm Y$ quadrant produces fits that increasingly differentiate between the quadrants, with increasingly favorable odds factors exceeding the simple 3-parameter model. When the $\pm Y$ quadrant becomes too small to contain enough events to constrain the parameters, the odds factor once more decreases. The model that maximizes the odds factor, entry 7, also differentiates the most

between the quadrants, with small parameter errors and close to 90% of GRBs in the core in each quadrant set. It is preferred over the all-sky core-plus-tail model by a factor of 16. This set of parameters defines $\pm Y$ quadrants with 45° azimuth in each quadrant and lower systematic errors for GRBs localized in these quadrants than for those in the $135^\circ \pm X$ quadrants. This quadrant definition also produces larger odds factors for the Ground-Auto localizations than the core-plus-tail model that has equal 90° quadrants, with the Ground-Auto providing an independent data set from the same GRB sample. This quadrant-dependent core-plus-tail model for the systematic uncertainty associated with GBM GRB localizations is illustrated in Figure 8. The figure shows how the probability of the systematic uncertainty changes as a function of angular offset from a GBM GRB localization for GRBs localized in the $\pm Y$ quadrants.

Core + Tail (2 Gaussians) varying the azimuth boundaries of the quadrants Version 4.14g of the HitL code with 212 reference locations and 100 IPN annuli										
#	Quadrants	Azimuth ranges	Core °	Error °	Core %	Error %	Tail °	Error °	Log ₁₀ Likeli- hood	Log ₁₀ Odds Factor
1	All-sky	0 - 360°	3.71	0.24	90.0	3.5	14.3	2.5	241.3	238.9
2	$\pm X$	315 - 45° and 135 - 225°	4.30	0.38	90.3	5.9	15.0	4.8	242.6	238.7
	$\pm Y$	45 - 135° and 225 - 315°	3.34	0.26	92.0	3.5	14.5	3.5		
3	$\pm X$	320 - 40° and 140 - 220°	4.23	0.52	87.2	7.7	14.1	4.8	242.6	238.8
	$\pm Y$	40 - 140° and 220 - 320°	3.47	0.25	93.6	3.3	15.5	3.6		
4	$\pm X$	305 - 55° and 125 - 235°	4.25	0.32	92.6	4.6	15.9	4.7	242.6	238.8
	$\pm Y$	55 - 125° and 235 - 305°	3.16	0.45	90.2	4.8	14.8	3.6		
5	$\pm X$	300 - 60° and 120 - 240°	4.32	0.29	93.4	4.0	16.2	4.9	243.9	240.1
	$\pm Y$	60 - 120° and 240 - 300°	2.59	0.40	86.6	6.1	13.5	3.2		
6	$\pm X$	295 - 65° and 115 - 245°	4.17	0.28	91.3	3.9	15.5	3.6	244.2	240.2
	$\pm Y$	65 - 115° and 245 - 295°	2.42	0.38	89.3	5.7	13.2	3.9		
7	$\pm X$	292.5 - 67.5° and 112.5 - 247.5°	4.17	0.28	91.8	3.9	15.3	3.6	244.2	240.3
	$\pm Y$	67.5 - 112.5° and 247.5 - 292.5°	2.31	0.39	88.4	6.4	13.2	3.8		
8	$\pm X$	290 - 70° and 110 - 250°	4.12	0.28	91.7	3.9	14.9	3.6	243.7	239.9
	$\pm Y$	70 - 110° and 250 - 290°	2.35	0.43	87.0	7.0	12.7	4.0		
9	$\pm X$	285 - 75° and 105 - 255°	3.96	0.26	89.9	3.8	15.3	2.9	243.0	239.4
	$\pm Y$	75 - 105° and 255 - 285°	2.64	0.54	90.7	10.6	9.1	4.8		

Table 5: Effect of varying the quadrant boundaries when assessing the quadrant-dependent core-plus-tail fit to the systematic uncertainty on GBM localizations.

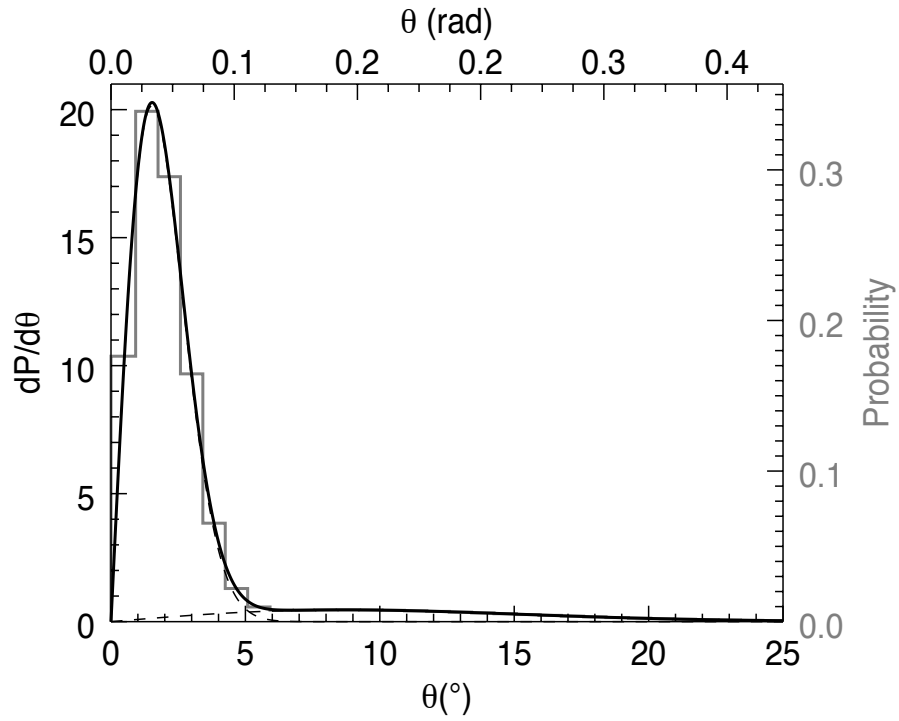


Fig. 8.— The solid curve shows the sum of the two components in the core and tail of a model representing the total 68% confidence level systematic uncertainty for GRBs localized in the $\pm Y$ quadrants in the spacecraft coordinate frame. The dashed curves show the individual components for the core and tail of the model. The histogram shows the probability of a systematic error for a given angular bin.

5.1. Flight Software systematic localization uncertainties

Both the Initial and Final FSW locations had sufficiently distant outliers ($> 90^\circ$) that most single component fits did not converge. Removing the five worst localizations allowed the fitting of several single component models for the Initial locations, shown in Table 6. The IPN annuli were also removed as it could not be determined for these reference locations which were the worst outliers and the fits failed to converge when they were included. The single-component fits for the FSW Initial locations are presented because these were the only fits that converged, and the parameter values may be useful, but it should be noted that these fits omit the five worst localizations.

Fits using the more complex core-plus-tail models converged using the entire FSW Final location sample (omitting the IPN set). These fits and the single component fits with a Z hemisphere dependence for the FSW Final locations, the only single-component model that converged with the entire sample, are reported in Table 7.

In September 2009, the *Fermi* rocking angle changed from 35° to 50° . The rocking angle change was necessary to keep the spacecraft battery cool, but one unfortunate effect on GBM is that more GRBs are viewed with an unfavorable detector geometry and the GBM localization quality may have suffered. Because of on-board hardware limitations, the full atmospheric scattering calculation performed on the ground is replaced by a standard model table for the atmospheric scattering contribution that assumes a zenith-pointed spacecraft. This becomes increasingly unrealistic with the updated rocking angle but the on-board limitations do not permit multiple tables that would cover several possible *Fermi* pointings. In order to assess the effect of this change on the FSW localizations, the FSW Final location sample was split into the 43 GRBs occurring before the change and the 149 since then. Table 8 shows a comparison of the systematic errors on these localizations. Single-component

FSW Initial Locations: Single Component models across hemispheres						
Model	Number GRB		Peak °	Error °	Log ₁₀ Likelihood	Log ₁₀ Odds Factor
	Point	Annuli				
Single	187	0	15.4	0.8	3.7	3.2
Hemisphere +X	187	0	12.2	1.2	5.5	4.9
-X			17.2	1.2		
Hemisphere +Y	187	0	12.7	1.0	6.0	5.4
-Y			18.2	1.4		
Quadrants ±X	187	0	19.7	1.6	7.5	6.9
±Y			12.5	0.9		

Table 6: Estimate of systematic uncertainty on the initial FSW localizations at 1.9 s post-trigger.

fits were possible with the smaller sample and only core-plus-tail modeling was possible with the larger sample. It appears the worst outliers have been detected since the rocking angle change and the value of the systematic error for the core is higher than the single model that best fits the sample localized before the rocking angle change. This suggests there has been a deterioration in the quality of the FSW localizations since September 2009.

5.2. The special case for short GRBs

Short GRBs (SGRB, duration < 2 s) are especially interesting to the follow-up community, both because they are rarer and because their putative association with the merger of a neutron star with either a neutron star (NS-NS) or a black-hole (NS-BH) is less well established than the connection between long GRBs and the collapse of massive stars. It is useful to characterize the systematic errors of the short GRB localizations in order to assess the regions with the maximum probability of containing the source or to calculate the probability that the GRB was in a region observed in another wavelength.

Only 22 of the 203 reference locations in our sample are for short GRBs, and an additional 13 SGRBs have narrow IPN annuli. The top panel of Figure 9 shows the reported 68% CL error on the GBM locations as a function of their offset from the real GRB position for the HitL localizations of the 22 SGRBs in our sample. The cumulative distribution of offsets from the true position appears in the bottom panel. Owing to the low fluences of SGRBs, they are typically localized with larger statistical uncertainties than long GRBs. The 68% and 90% containment radii of the true positions from the GBM positions are 8.7° and 16.1° , respectively, but with large uncertainties owing to the small sample size. There is a steep rise in containment of the true source position at just under 6° from the GBM position after which it remains flat, though with 22 events this curve may also result from small statistics. Covering an area 6° around the reported position might be a good strategy, regardless of the reported error on the localization, which is only weakly correlated with the true source offset for these short events. Ground-automated localizations of SGRBs are displayed in the same way in Figure 10. It can be seen that although the containment radii are higher (10.5° and 26.5° for the 68% and 90% sample containment), there is a similar steep rise at just under 6° from the position reported by GBM so that with a limited FoV, observers would capture 50% of the true positions using a search radius of 6° .

More short GRBs with known positions are required to characterize the systematic error on these events convincingly. A preliminary analysis of the HitL 4.14g locations for SGRBs using our Bayesian code, which uses 13 IPN annuli in addition to the 22 reference locations, suggests a single-component systematic uncertainty of $7.0 \pm 1.0^\circ$. A core-plus-tail model

Core + Tail fits to the systematic uncertainty on the FSW Final locations											
Type	Hemisphere	Number GRB		Core	Error	Core	Error	Tail	Error	Log ₁₀	Log ₁₀
		Point	Annuli	°	°	%	%	°	°	Likelihood	Odds Factor
Quadrant	All-sky	192	0	7.52	0.76	89.7	2.9	55.6	9.0	39.6	38.1
	±X	192	0	8.29	1.34	85.7	6.2	59.6	12.9		
	±Y			7.35	1.03	92.9	3.7	62.6	18.5	40.1	38.5
Hemi	+X	192	0	5.99	1.12	86.3	4.6	47.2	9.0	40.4	38.5
	-X			8.80	1.02	92.2	3.4	68.2	27.2		
Hemi	+Y	192	0	7.84	1.16	92.4	4.9	35.6	12.3	41.3	39.5
	-Y			6.66	1.17	84.3	4.8	62.2	13.2		
The Z-hemisphere model failed to converge. The Z-hemisphere-dependent single component is below.											
Single	+Z	192	0	12.18	0.7					13.0	12.6
	-Z			34.09	2.71						

Table 7: Estimate of systematic uncertainty on the last-issued FSW localizations.

Effect of rocking angle change on FSW localization systematic uncertainty									
Type	Hemisphere	Core	Error	Core	Error	Tail	Error	Log ₁₀	Log ₁₀
		°	°	%	%	°	°	Likelihood	Odds Factor
FSW Final locations for 43 GRBs in initial rocking profile									
All-sky		5.80	0.99					25.3	24.9
Hemi	+Y	4.52	1.39					25.6	25.2
	-Y	6.98	1.58						
Quad	±X	8.10	1.79					26.2	25.9
	±Y	3.82	1.26						
FSW Final locations for 149 GRBs since the rocking angle change									
All-sky		8.32	1.01	87.0	3.8	56.6	9.8	17.1	15.9
Hemi	+X	7.59	1.32	84.0	5.7	48.8	10.1	17.3	15.9
	-X	9.14	1.26	89.9	4.6	67.7	27.0		
Hemi	+Y	10.21	1.46	95.1	5.4	48.2	29.6	19.0	18.0
	-Y	6.18	1.77	79.9	6.3	60.1	12.6		
Hemi	+Z	7.52	1.42	93.1	5.4	42.4	15.9	21.0	20.1
	-Z	10.40	2.32	67.3	9.9	63.0	14.8		
Quad	±X	7.93	1.63	78.5	7.4	52.6	10.7	17.8	16.8
	±Y	9.26	1.09	93.3	3.8	71.9	51.7		

Table 8: Effect of rocking angle change on the quality of FSW final locations. The systematic error for the sample of 43 GRBs before the spacecraft rocking angle increased from 35° to 50° is modeled by a single Gaussian. More complicated models failed to converge, possibly owing to the small sample size. For the 149 GRBs detected after the rocking angle change, only the core-plus-tail models converged, probably because the systematic errors associated with the tail of the population were too large for a single-component model to result in an acceptable fit.

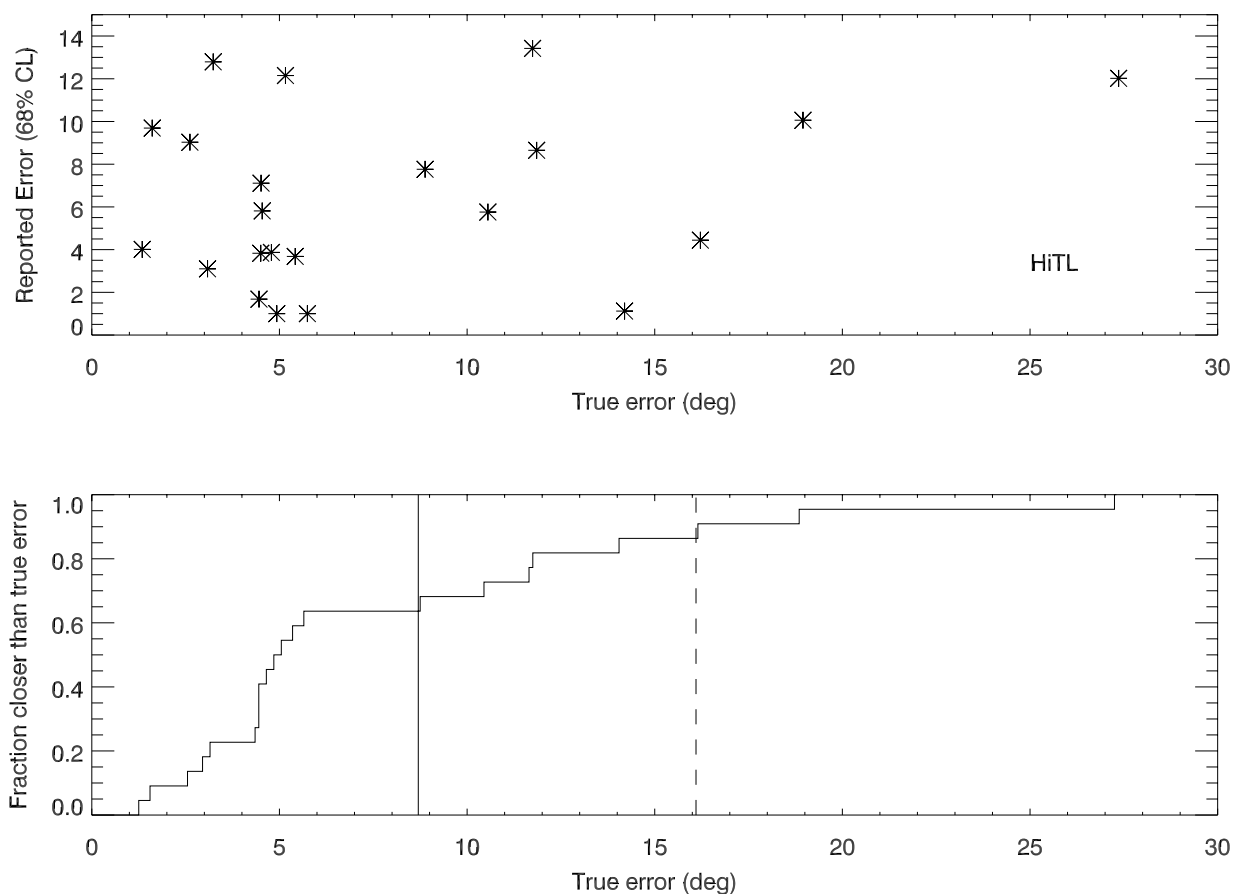


Fig. 9.— The reported 68% CL uncertainty for 22 short GRBs localized by GBM is shown in the top panel as a function of the true offset. The histograms show the fraction of GBM HitL localizations lying within a given offset (degrees) from the true position. The solid vertical line indicates the 68% containment radius 8.7° and the dashed vertical line the 90% radius of 16.1° . The 68% containment region for the 68% containment radius for the HiTL locations lies between 5.3 and 11.7° with the 90% containment radius having a lower limit of 11.6° and being unconstrained at the upper end.

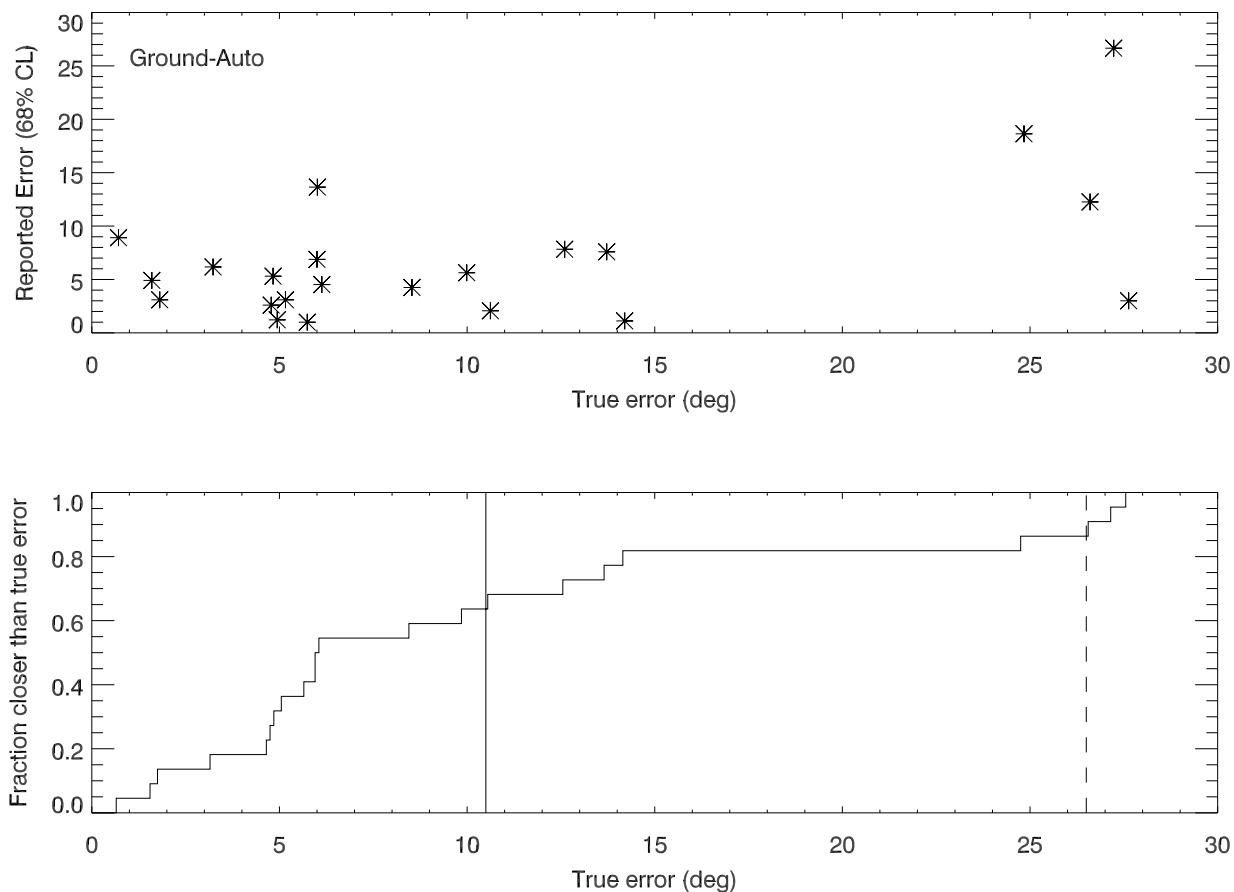


Fig. 10.— The reported 68% CL uncertainty for 22 short GRBs localized by GBM using the ground-automated process is shown in the top panel as a function of the true offset. The histograms show the fraction of GBM Ground-Auto localizations lying within a given offset (degrees) from the true position. The solid vertical line indicates the 68% containment radius 10.5° and the dashed vertical line the 90% radius of 26.5° . The 68% containment region for the 68% containment radius for the Ground-Auto locations lies between 8.4 and 14.1° with the 90% containment radius having a lower limit of 13.6° and being unconstrained at the upper end.

with $4.7 \pm 1.0^\circ$, a core fraction of $78 \pm 2\%$ and a tail component of $12 \pm 5^\circ$ is mildly preferred and suggests the short burst systematic uncertainties are compatible with those of the GRB population as a whole, with the exception that the fraction in the tail is higher. This could explain the larger systematic uncertainty obtained in the single-component model for the short bursts compared to the population as a whole ($5.2 \pm 0.2^\circ$). Attempts to characterize the systematic uncertainty associated with the Ground-Auto localizations fail with this small sample. The sample of SGRBs with IPN annuli can be increased using the large number of SGRBs seen only by GBM and Konus-Wind (Pal’shin et al. 2013).

5.3. Applying the model to the data

Figure 5 showed that only 39% of the HitL localizations fell within the $1\sigma_{stat}$ statistical uncertainty region of the true reference location, σ_{stat} , with 70% within $2\sigma_{stat}$. If we convolve the statistical uncertainty, assuming circular uncertainty regions, with the best-fit quadrant-dependent core-plus-tail model of the systematic uncertainty, σ_{sys} , explored in Section 5, adding the functions in quadrature $\sigma_{tot} = \sqrt{(\sigma_{stat}^2 + \sigma_{sys}^2)}$, then we find that 67.5% lie within the $1\sigma_{tot}$ radius and 94.5% within $2\sigma_{tot}$. If instead of the circular assumption we make for σ_{stat} we convolve the χ^2 map with the model for the systematic uncertainty that was found to be the best fit of those we explored in Section 5, these numbers are 68.7% and 91.4%, respectively. Similar results are found for the Ground-auto localizations. Propagating the uncertainties on the model parameters produces a variation of 1-2% in these containment percentages.

6. Summary and future plans

Using a reference sample of 203 GRBs with known locations we have found that ground-automated GBM localizations distributed as Ground Position GCN notices between 30 s and about a minute after the trigger time lie within 7.6° of the true location 68% of the time and within 17.2° 90% of the time (Figure 4). These numbers are for the population as a whole and do not take into account the reported statistical uncertainty. For GRBs with small statistical localization uncertainties of 1° this improves to $2.2 - 5.6^\circ$ for the 68% containment level, with the sample of GRBs with localization errors this small insufficient to determine the 90% containment level (Figure 6). The localizations produced with human intervention (HitL) that are distributed as Final Position GCN notices 30 min to hours after the trigger are within 5.3° and 10.1° of the true position for 68% and 90% of GRBs, respectively. For GRBs with statistical localization uncertainties of 1° the 68% containment radius is $3.3 - 4.7^\circ$

with the sample again too small to determine the 90% containment radius.

An analysis of the systematic uncertainty on GBM localizations that takes into account the reported statistical uncertainty used, in addition to the 203 point locations, 100 IPN annuli and 9 IPN intersecting annuli that are treated as point locations, for a total of 312 reference locations. The model that best represents the systematic uncertainty for both the automated and HitL localizations includes a core component and a tail component. For the Ground-Auto, the core component is a Gaussian that peaks at $3.7 \pm 0.3^\circ$ and contains about 80% of the GRB locations, with a Gaussian tail peaked at $14 \pm 2^\circ$. The HitL systematic uncertainty has similar values but 90% of the localizations are contained in the core (Table 3). Both localization types show evidence for a dependence of the error on the GRB position in spacecraft coordinates, with bursts incident near the $\pm Y$ -axes better localized than those near the $\pm X$ -axes (Table 4). With three extra parameters, the size of the reference sample is not large enough for this model to be preferred statistically. Modifying the azimuthal area covered in these X- and Y- axes produces a model for the HitL localizations that is preferred over the simpler core-plus-tail model described above (Table 5). Because the parameters in this model are well-constrained and the results are reproduced using the Ground-Auto localizations, we consider this a good model for the systematic uncertainty of GBM-localized GRBs.

Applying this model to the data, using either the circular approximation to σ_{stat} that was input to the Bayesian model or the actual χ^2 -grid values to define the statistical confidence levels, resulted in the containment percentages of the the reference locations within the expected total uncertainty regions.

The quality of our localization depends on the quality of the model rates that we compare with our observed rates. This in turn relies on our knowledge of the detector responses both to the direct flux and to the scattered flux from both the spacecraft and the atmosphere. Systematic effects owing to a poor choice of model spectrum may contribute to a poor localization, as can inaccuracies in our detector response, our mass model of the Fermi spacecraft, and our model of scattering from the atmosphere. The dependence of the systematic uncertainty in our localization on the position of the GRB in spacecraft coordinates may offer clues to the major sources of these systematic errors. A systematic error that was dominated by our detector responses or by inaccuracies in our atmospheric scattering modeling is unlikely to exhibit such a dependence on position in spacecraft coordinates, although both of these factors may play a part. The $\pm X$ sides of the spacecraft contain much of the wiring and electronics boxes, with the -X side also housing the star trackers. By contrast, the $\pm Y$ sides, housing the LAT radiators and solar panels, are clearer of material. The quadrant dependence of σ_{sys} implies that the bursts incident on parts of the spacecraft with

fewer electronics boxes and large cable bundles have better localizations than those arriving on a busier part of the spacecraft. This may imply inaccuracies in our mass model lead to a miscalculation of the observed rates that arise from scattering in the spacecraft. We will explore the possibilities of improving this model in future work.

The localization of short GRBs is poorer than long GRBs, with 68% localized within $5.3 - 11.7^\circ$ of the true position when humans are involved and $8.4 - 14.1^\circ$ in the automated process. The sample is small so these containment radii have large uncertainties. An analysis of the systematic uncertainty on the HitL locations of short bursts finds it is similar to long bursts, suggesting the difference is owed to the poorer statistics associated with fewer counts. Figures 9 and 10 show that the large values may be attributable to outliers and that 50% of both HitL and Ground-Auto localizations of short GRBs are contained within 6° of the true location.

Flight software locations suffer larger statistical and systematic uncertainties and are useful mainly to assist the LAT onboard science algorithms and to initiate repointings of the spacecraft in response to bright GRBs (Figure 2 and Tables 6 and 7). The quality of FSW localizations has significantly declined following the rocking profile change of *Fermi* in September 2009 (Table 8) and we will endeavor to mitigate this deterioration, with enhancements subject to the limitations of onboard processing.

Improving the Ground-Auto localization to approach the quality of the HitL localization is a priority, with the first goal to replace the peak flux localizations, which use MAXRATES packets, with fluence localizations using the entire count-rate time series as it arrives in real-time. This should reduce the statistical component to the localization uncertainty on the Ground-Auto positions. Identifying outliers in the automated process could also help, particularly for the short GRBs, which will not be significantly improved by the implementation of a fluence localization.

The GCN localization notices currently report a 68% confidence-level statistical uncertainty that assumes a circular region around the χ^2 minimum position. In practice, the σ_{stat} contours can be elliptical or irregular depending on the χ^2 map returned in the minimization process. We have implemented an algorithm to convolve the χ^2 map with an input systematic uncertainty model to return 1σ , 2σ , and 3σ contour maps for our localizations. An example is shown in Figure 11. The contours returned by the localization process can be ragged. They are overplotted on the smoothed contours with which the systematic uncertainty, modeled as the sum of two quadrant-dependent Fisher functions described above, has been convolved. As the systematic error is better characterized, and hopefully improved, the model parameters are easily modified to return the contours that best represent the current knowledge of the localization quality. We started delivering these contour maps to the com-

munity in January 2014. They are used regularly by the iPTF team in follow-up observations that have led to the discovery of seven GRB afterglows. The maps are available at the *Fermi* Science Support Center ¹ in ascii, png, and FITS format. Because of the real-time delivery limitations of the GCN and processing and transfer latency to the FSSC, the contours are available at the *Fermi* Science Support Center from 30 minutes to a couple of hours after the GRB trigger.

We thank an anonymous referee for very useful contributions to this paper. The GBM project is supported by NASA. Support for the German contribution to GBM was provided by the Bundesministerium für Bildung und Forschung (BMBF) via the Deutsches Zentrum für Luft und Raumfahrt (DLR) under contract number 50 QV 0301. A.v.K. was supported by the Bundesministeriums für Wirtschaft und Technologie (BMWi) through DLR grant 50 OG 1101. HFY acknowledges support by the DFG cluster of excellence “Origin and Structure of the Universe”. AG and SG are funded through the NASA Postdoctoral Fellowship Program. SF acknowledges the support of the Irish Research Council for Science, Engineering, and Technology, co-funded by Marie Curie Actions under FP7. GF acknowledges the support of the Irish Research Council. DT acknowledges support from Science Foundation Ireland under grant number 09-RFP-AST-2400.

¹<http://fermi.gsfc.nasa.gov/gbm>

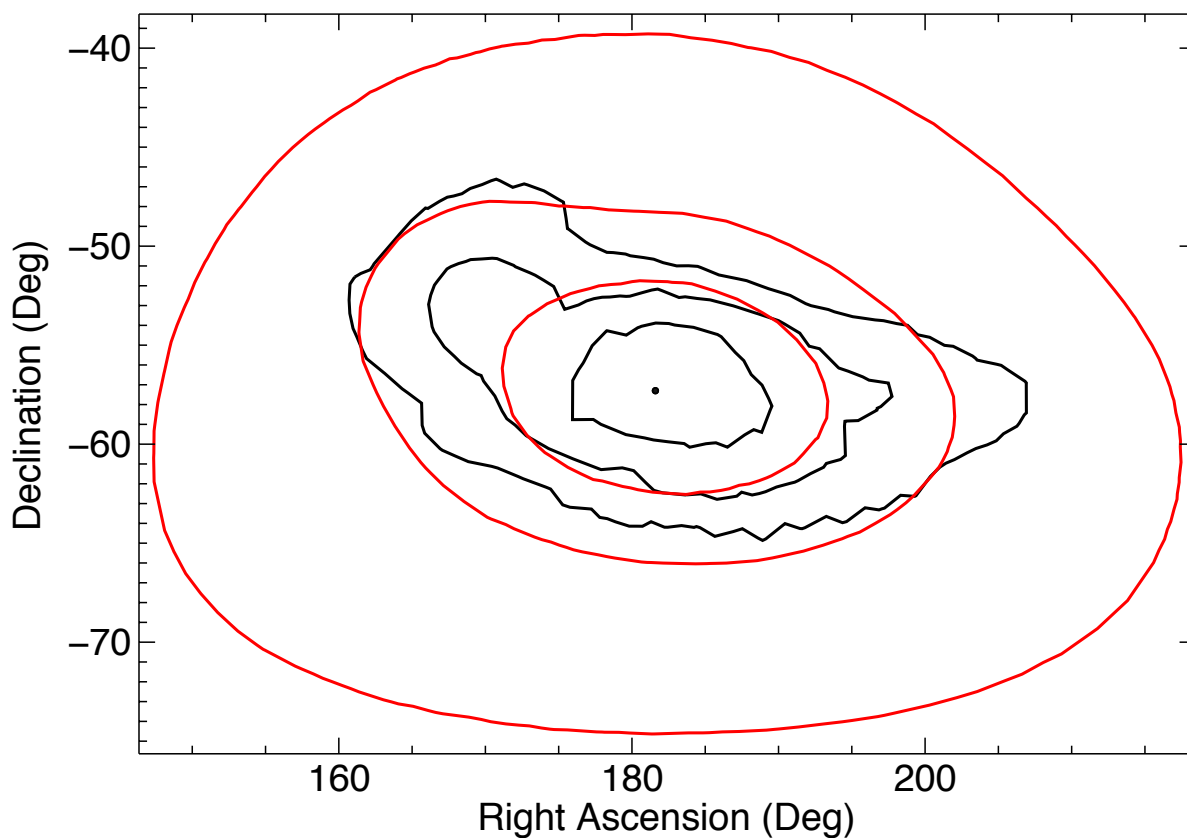


Fig. 11.— The 1σ , 2σ , 3σ contours for GRB 080714745. The black contours are the statistical uncertainty σ_{stat} , returned by the localization process. After convolving with the best-fit model for the systematic uncertainty, σ_{sys} , described in the text as a sum of core-plus-tail Fisher functions with parameters that vary according to the quadrant in which the GRB is localized, the red curves are obtained, $\sigma = \sqrt{(\sigma_{stat}^2 + \sigma_{sys}^2)}$.

A. Distributions of χ^2 for GBM GRB localizations

A grid of 41168 possible arrival directions in a spacecraft coordinate system, 1° apart, contains the expected count rates in each of the 12 NaI detectors for a burst originating from that direction. The relative count rates in the 12 detectors depend not just on the arrival direction but also on the energy spectrum of the gamma-ray source. Minimizing χ^2 on the grid of 41168 possible arrival directions based on the observed count rates from a GRB yields the best fit arrival direction for that assumed spectral shape.

For each of 41168 positions in the grid, i , we find

$$\chi^2(i) = \sum_{j=1}^{12} \frac{[s(j) - b(j) - f(i) * m(j, i)]^2}{b(j) + f(i) * m(j, i)} \quad (\text{A1})$$

where $s(j)$ and $b(j)$ are the total observed and background rates, respectively, observed between 50 and 300 keV in detector j ; $m(j, i)$ are the model rates in the same energy range for detector j in row i ; and $f(i)$ is the normalization factor for row i such that

$$f(i) = \frac{\sum_{j=1}^{12} [m(j, i) * (s(j) - b(j))]/s(j)}{\sum_{j=1}^{12} m(j, i)^2/s(j)} \quad (\text{A2})$$

We try three different spectral models representing soft, medium, and hard GRB spectra, as described in section 2. The direction yielding the lowest χ^2 may vary according to the spectral model, so we obtain up to three possible arrival directions, one for each model. The spectral model returning the lowest χ^2 is assumed to be the better fit to the data and the code therefore selects the position yielding the lowest χ^2 across all three models as the most likely arrival direction for the GRB.

In the reference sample that includes the 203 reference locations from other satellites and the 110 locations from the IPN, the location from the hard spectrum model table is selected 16% of the time, the medium 53% and the soft 31%. The medium and soft GRB spectral models produce the same burst arrival direction for 33% of the sample and only two GRBs are localized to the same grid point under all three spectral models. There are no cases where the hard and soft spectra produce the same χ^2 minimum arrival direction but where those directions are different from those obtained under the assumption of the medium GRB spectrum. The use of three spectral models thus produces different optimal arrival directions for 2/3 of the GRB reference sample. The statistical preference for the soft or medium tables

over the hard table or vice versa typically involves tens of units of χ^2 whereas the selection of soft over medium or vice versa typically involves fewer than 20 units of χ^2 . Using any of the three models individually for the whole sample results in poorer localizations overall, as determined by both a larger median distance to the true location for the whole sample and a larger value for the systematic error calculated as described in section 5. This suggests the assumed source spectrum does affect the quality of the localization. We have tried different spectral models, working from the distribution of measured catalog values for Band function parameters (Goldstein et al. 2012; Gruber et al. 2014) but have thus far not obtained a significant improvement relative to the methods and models currently being used that are described in this paper. This was somewhat surprising given that the assumed spectral shapes (particularly the hard spectrum) are extreme compared to the measured spectral shapes. We also expect that because of the scattering of high-energy photons off material in the spacecraft into the 50 - 300 keV energy range used for the localization process, systematic effects arising from inaccuracies in the spacecraft mass model in our simulations result in spectrally harder bursts being more poorly localized than bursts with a softer spectrum. Quantifying the effect by dividing the GRB sample, for example by hardness ratios or E_{peak} values, is complicated by the fact that short GRBs are spectrally harder, have lower fluences (and hence larger statistical uncertainties), and are underrepresented in the GRB sample with reference locations. The effects of spectral modeling on source localization are still being explored and will be reported in a future paper.

Localization uncertainties for dim GRBs are dominated by statistics. Bright bursts have low statistical uncertainties and their χ^2 values become larger with increasing intensity as the goodness of fit is affected by systematics. Figure 12 shows the distribution of minimized χ^2 values for the reference sample and the dependence of this value on the brightness of the GRB, represented by the significance above the background of the data used in the localization. Figure 13 shows the same quantities but with the minimum χ^2 calculated after normalizing the observed data rates to those of a GRB of average intensity (1 photons/cm²/s between 50 and 300 keV). The dependence of the minimum χ^2 on source intensity disappears for bright GRBs ($> 20\sigma$ above background) but the weaker bursts now show higher normalized χ^2 values, probably because the quality of the localization depends more on the quality of the fit to the background data than for brighter GRBs, and systematics due to poor background fitting are magnified by the normalization of the source rates upwards to a GRB of average intensity. In the localization process, we use the normalized χ^2 to assess the goodness-of-fit of the localization, rejecting localizations with normalized χ^2 values above 500 as bad fits. This threshold was found to be efficient in rejecting triggered events due to particle precipitation, which do not have relative detector rates consistent with a point on the sky, without rejecting GRBs with poor localizations. The normalization process does not affect

either the determination of the arrival direction, the spectral model that is selected, or the reported localization uncertainty that is calculated based on observed rather than normalized count rates.

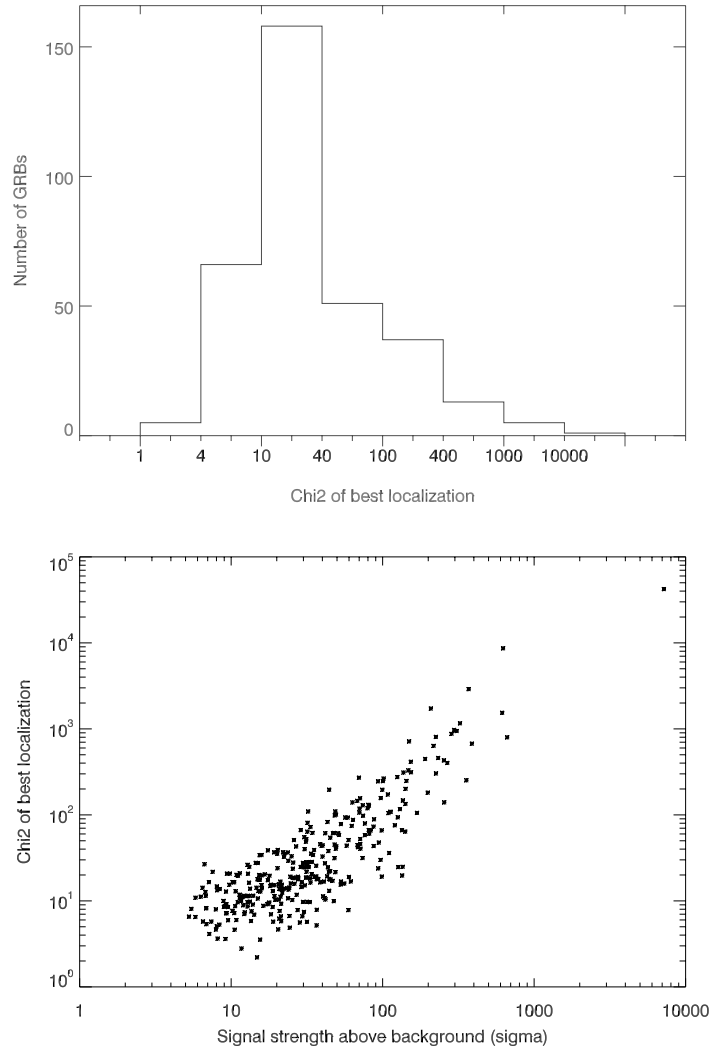


Fig. 12.— The top panel shows the distribution of minimum χ^2 values for the GBM localizations of the sample of GRBs with reference and IPN locations. There is a strong correlation with the intensity of the GRB, as seen in the lower panel which shows the variation of χ^2 with the strength of the data signal used in the minimization.

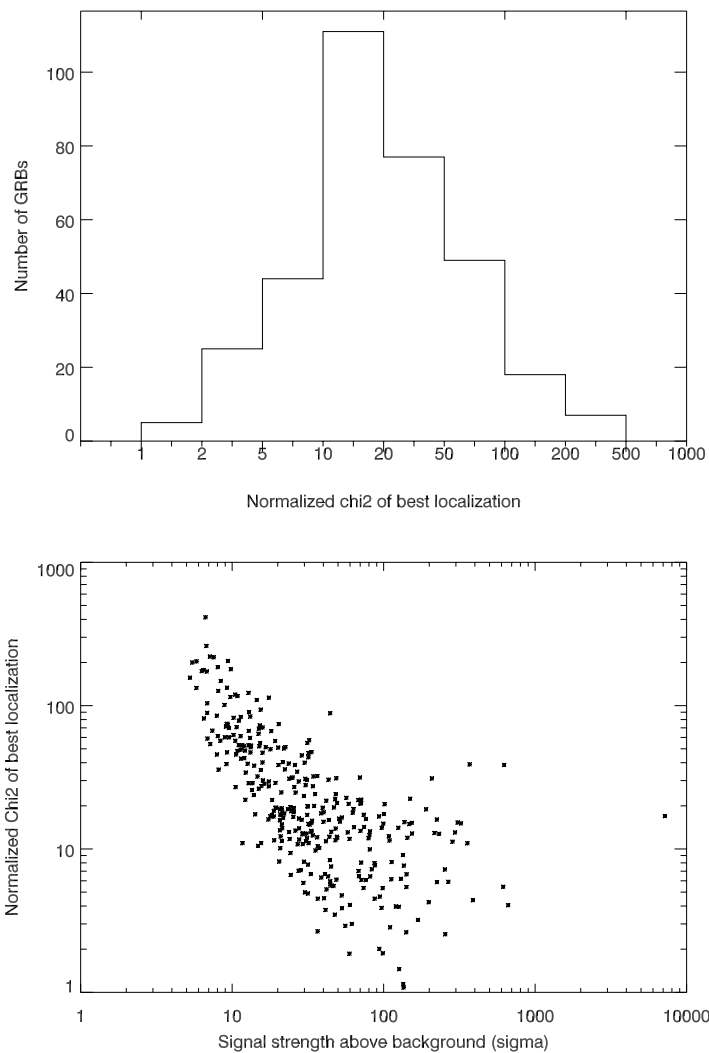


Fig. 13.— The top panel shows the distribution of minimum χ^2 values for the GBM localizations of the sample of GRBs with reference and IPN locations after normalizing the intensity of the GRB (i.e., the observed counts that were used in the minimization) to a fiducial burst of average intensity. The correlation of χ^2 with source signal shown in Figure 12 is reversed (lower panel), with the weaker bursts showing higher values of χ^2 , probably because poor fits to the background count rates are magnified in the normalization process and affect the goodness-of-fit of the localization.

B. Reference locations

Table 9: 203 reference locations for GRBs that were also detected by GBM and which we use to assess the accuracy of GBM locations. These locations come from *Swift* BAT, *Swift* XRT, *Fermi*-LAT, INTEGRAL, MAXI, Super-AGILE, and the IPN. All RA, Dec, and Err are in units of degree.

Burst Name	Common Name	Trigger Time (UT)	FSW _{first} for Ref.			FSW _{last} for Ref.			Ground Auto for Ref.			H.i.t.L for Ref.			Ref. Location			Reference	
			(RA)	(Dec)	(Err)	(RA)	(Dec)	(Err)	(RA)	(Dec)	(Err)	(RA)	(Dec)	(Err)	(RA)	(Dec)	(Err)		(RA)
080714745	GRB 080714A	17:52:54.03	-	-	-	-	-	-	185.3	-57.7	3.8	183.5	-57.5	3.9	188.1	-60.2	3.0	176.8	Barthelmy et al., GCN 7979
080723557	GRB 080723B	13:22:21.38	-	-	-	-	-	-	177.6	-58.8	1.2	175.1	-60.7	1.0	176.8	-60.2	1.0	176.8	Gotz et al., GCN 8002
080725435	GRB 080725A	10:26:09.06	-	-	-	-	-	-	120.2	-13.4	4.1	123.1	-23.1	2.2	121.7	-14.0	2.2	121.7	Krimm et al., GCN 8014
080727964	GRB 080727C	23:07:46.22	-	-	-	-	-	-	43.5	59.8	4.2	40.0	62.2	2.7	32.6	64.1	2.7	32.6	Fenimore et al., GCN 8044
080804972	GRB 080804A	23:20:14.88	-	-	-	-	-	-	324.1	-52.7	3.9	320.8	-52.7	2.4	328.7	-53.2	2.4	328.7	Markwardt et al., GCN 8067
080810549	GRB 080810A	13:10:12.59	-	-	-	-	-	-	358.3	-5.7	5.0	355.8	5.5	2.2	356.8	0.3	2.2	356.8	Sakamoto et al., GCN 8082
080905499	GRB 080905A	11:58:55.04	-	-	-	-	-	-	282.5	-12.0	4.3	287.0	-20.0	4.1	287.7	-18.9	4.1	287.7	Cummings et al., GCN 8187
080905705	GRB 080905B	16:55:46.85	-	-	-	-	-	-	291.7	-56.2	6.1	307.7	-62.1	5.8	301.7	-62.6	5.8	301.7	Barthelmy et al., GCN 8188
080916009	GRB 080916C	00:12:45.62	-	-	-	-	-	-	124.3	-54.3	2.5	124.4	-54.7	1.4	119.8	-56.6	1.4	119.8	Tajima et al., GCN 8246
080916406	GRB 080916A	09:45:18.94	-	-	-	-	-	-	334.3	-57.1	3.2	335.3	-56.4	2.2	336.3	-57.0	2.2	336.3	Baumgartner et al., GCN 8243
080928628	GRB 080928A	15:04:56.05	-	-	-	-	-	-	132.3	-73.7	12.5	97.8	-50.0	4.0	95.1	-55.2	4.0	95.1	Fenimore et al., GCN 8297
081008832	GRB 081008A	19:58:01.80	257.9	-47.6	22.8	296.9	-46.2	14.4	273.1	-50.9	7.2	274.4	-53.8	3.4	280.0	-57.5	3.4	280.0	Racusin et al., GCN 8344
081012549	GRB 081012A	13:10:23.04	22.3	-32.5	17.6	28.9	-25.4	11.6	36.7	-12.8	7.1	27.2	-11.2	5.6	30.2	-17.6	5.6	30.2	Sato et al., GCN 8344
081024245	GRB 081024A	05:53:09.01	38.4	55.2	25.3	38.4	55.2	25.3	34.3	62.5	6.2	34.3	62.5	12.8	27.9	61.3	12.8	27.9	Barthelmy et al., GCN 8404
081024891	GRB 081024B	21:22:40.87	317.8	20.7	20.0	317.8	20.7	20.0	320.3	17.1	5.4	319.6	17.9	5.9	322.9	21.2	5.9	322.9	Omodei, GCN 8407
081025349	GRB 081025A	08:23:05.30	225.1	57.5	15.4	241.3	55.3	7.2	240.6	56.3	2.2	245.9	56.8	3.2	245.3	60.5	3.2	245.3	Copete et al., GCN 8409
081101491	GRB 081101A	11:46:32.06	93.6	10.9	14.3	93.6	10.9	14.3	89.9	0.9	13.7	80.8	11.6	10.1	95.8	-0.1	10.1	95.8	Barthelmy et al., GCN 8458
081102739	GRB 081102A	17:44:21.60	326.8	57.8	18.9	318.8	61.6	15.8	303.6	56.1	7.8	321.3	51.9	4.5	331.2	53.0	4.5	331.2	Fenimore et al., GCN 8468
081109293	GRB 081109A	07:02:02.42	327.6	-52.4	29.3	320.8	-49.6	18.0	310.7	-57.3	10.6	331.5	-51.9	3.5	330.8	-54.7	3.5	330.8	Markwardt et al., GCN 8507
081121858	GRB 081121A	20:35:27.76	106.9	-67.4	18.1	101.4	-62.4	5.8	78.1	-53.3	2.9	97.2	-59.9	1.1	89.3	-60.6	1.1	89.3	Sakamoto et al., GCN 8539
081126899	GRB 081126A	21:34:09.07	331.7	43.0	6.4	331.9	43.0	6.5	327.3	47.8	1.5	326.9	50.3	2.7	323.5	48.7	2.7	323.5	Sato et al., GCN 8557
081221681	GRB 081221A	16:21:12.22	21.7	-19.6	11.9	18.3	-21.7	4.2	14.6	-23.9	1.6	14.1	-25.2	1.2	15.8	-24.5	1.2	15.8	Cummings et al., GCN 8708
081222204	GRB 081222A	04:54:00.26	34.1	-26.4	7.0	29.4	-30.6	5.0	18.6	-32.4	2.0	18.6	-32.4	1.5	22.7	-34.1	1.5	22.7	Fenimore et al., GCN 8709
081226044	GRB 081226A	01:03:37.53	90.4	-59.5	15.2	90.4	-59.5	15.2	121.2	-68.3	9.0	124.2	-68.0	9.7	120.5	-69.0	9.7	120.5	Krimm et al., GCN 8735
081226509	GRB 081226B	12:13:10.71	49.4	-46.2	18.5	49.4	-46.2	18.5	26.4	-53.3	6.9	13.5	-51.6	7.8	25.5	-47.4	7.8	25.5	Merghetti et al., GCN 8734
090102122	GRB 090102A	02:55:30.85	122.9	26.4	9.5	133.6	28.6	5.2	130.1	29.8	1.5	128.5	30.3	1.5	128.2	33.1	1.5	128.2	Sakamoto et al., GCN 8769
090107681	GRB 090107B	16:20:42.77	161.0	86.0	26.1	288.8	47.1	9.0	287.9	51.3	6.8	285.9	53.3	11.4	284.8	59.6	11.4	284.8	Gotz et al., GCN 8786
090113778	GRB 090113A	18:40:40.85	31.2	35.1	8.2	31.2	35.1	8.2	26.4	32.7	7.6	29.0	38.5	8.6	32.1	33.4	8.6	32.1	Tueller et al., GCN 8808
090117640	GRB 090117A	15:22:01.06	173.9	-62.7	9.1	173.9	-62.7	9.1	175.0	-65.3	8.0	165.1	-63.2	7.0	164.0	-58.2	7.0	164.0	Donnarumma et al., GCN 8817
090129880	GRB 090129A	21:07:15.43	264.6	-37.4	7.1	264.7	-37.4	6.8	268.7	-32.6	1.5	270.6	-33.8	1.8	269.1	-32.8	1.8	269.1	Barthelmy et al., GCN 8862
090217206	GRB 090217A	04:56:42.56	210.3	-2.6	8.2	207.5	1.1	4.8	207.8	-5.3	1.6	211.3	-11.6	1.0	204.9	-8.4	1.0	204.9	Ohno et al., GCN 8903
090323002	GRB 090323A	00:02:42.63	190.7	20.8	5.2	184.2	21.4	5.8	190.0	20.8	1.3	190.1	21.1	1.2	190.7	17.1	1.2	190.7	Ohno et al., GCN 9021

Burst Name	Common Name	Trigger Time (UT)	FSW _{first} for Ref.		FSW _{last} for Ref.		Ground Auto for Ref.		H.i.t.L. for Ref.		Ref. Location		Reference				
			(RA Dec)	(Err)	(RA Dec)	(Err)	(RA Dec)	(Err)	(RA Dec)	(Err)	(RA Dec)	(Err)					
090328401	GRB 090328A	09:36:46.52	79.3	-46.7	26.3	80.0	-45.6	5.3	95.0	-44.5	2.1	95.9	1.0	90.9	-42.0	McEnery et al., GCN 9044	
090422150	GRB 090422A	03:35:17.07	296.9	36.1	18.4	296.9	36.1	18.4	297.7	42.1	8.5	296.3	10.3	294.7	40.4	Markwardt et al., GCN 9195	
090423330	GRB 090423A	07:55:25.40	151.3	11.0	31.9	151.3	11.0	31.9	144.5	9.1	50.0	154.9	13.5	148.9	18.2	Palmer et al., GCN 9204	
090424592	GRB 090424A	14:12:08.67	177.4	8.0	3.5	177.3	7.8	3.6	191.4	18.0	1.0	191.5	18.1	189.5	16.8	Sakamoto et al., GCN 9231	
090509215	GRB 090509A	05:10:05.72	220.2	-36.7	26.0	241.9	-28.8	15.5	237.5	-27.7	10.1	230.1	-27.7	241.4	-28.4	Tueller et al., GCN 9335	
090510016	GRB 090510A	00:22:59.98	340.8	-33.3	4.0	340.8	-33.3	4.0	335.1	-31.3	1.3	335.0	-31.3	333.6	-26.6	Ukwattia et al., GCN 9337	
090516353	GRB 090516A	08:27:58.35	139.4	-10.7	24.9	139.5	-0.5	15.0	141.6	-12.8	7.9	138.5	-14.8	1.1	138.2	-11.9	Baumgartner et al., GCN 9384
090518080	GRB 090518A	01:54:44.52	122.5	13.6	14.9	122.5	13.6	14.9	123.5	4.2	10.5	112.5	1.2	8.1	119.9	0.8	Cummings et al., GCN 9393
090519881	GRB 090519A	21:08:45.88	142.2	3.1	20.6	142.2	3.1	20.6	140.3	0.9	8.5	139.8	-5.4	5.2	142.3	0.2	Krimm et al., GCN 9406
090531775	GRB 090531B	18:35:56.50	250.0	-43.8	7.3	250.0	-43.8	7.3	254.0	-35.4	5.0	252.9	-31.5	7.2	252.1	-36.0	Cummings et al., GCN 9461
090618353	GRB 090618A	08:28:26.66	304.6	52.9	7.0	296.2	77.1	3.5	295.1	80.8	1.0	288.4	80.0	1.0	294.	78.4	Baumgartner et al., GCN 9530
090621185	GRB 090621A	04:26:34.49	12.7	44.1	21.1	3.4	61.2	14.3	3.6	60.8	5.4	8.7	60.8	2.4	11.0	61.9	Cummings et al., GCN 9534
090621922	GRB 090621B	22:07:25.71	341.4	63.9	14.7	341.4	63.9	14.7	348.1	67.9	7.9	320.7	68.9	9.1	313.4	69.0	Krimm et al., GCN 9551
090625560	GRB 090625B	13:26:22.52	19.4	-64.6	29.1	16.3	-59.8	13.5	0.1	-65.1	6.7	359.8	-69.2	5.2	2.3	-65.8	Goetz et al., GCN 9572
090626189	GRB 090626A	04:32:08.89	170.0	-36.6	4.8	170.6	-35.5	3.9	169.9	-35.3	1.0	169.6	-35.8	1.0	170.0	-33.5	Piron et al., GCN 9584
090712160	GRB 090712A	03:51:00.35	79.9	14.1	34.8	79.9	14.1	34.8	55.0	22.4	26.2	72.8	20.2	5.6	70.1	22.5	Mereghetti et al., GCN 9620
090704242	GRB 090704A	05:47:48.19	211.4	4.5	22.9	214.8	17.7	11.9	213.6	25.3	6.7	207.9	25.3	2.7	208.2	22.8	Palmer et al., GCN 9623
090708152	GRB 090708A	03:38:18.46	150.5	22.8	27.0	150.5	22.8	27.0	140.8	21.0	16.6	150.8	24.2	13.6	154.6	26.6	Ukwattia et al., GCN 9641
090709630	GRB 090709B	15:07:41.14	76.6	64.3	19.4	65.4	66.8	9.9	60.4	65.7	4.8	88.5	63.8	6.6	93.5	64.1	Barthelmy et al., GCN 9660
090712160	GRB 090712A	03:51:00.35	79.9	14.1	34.8	79.9	14.1	34.8	55.0	22.4	26.2	72.8	20.2	5.6	70.1	22.5	Cummings et al., GCN 9688
090813174	GRB 090813A	04:10:42.60	247.2	82.7	4.7	246.9	82.7	6.3	91.4	84.7	2.1	40.2	86.0	5.1	225.1	88.6	Evans et al., GCN 9699
090817036	GRB 090817A	00:51:26.21	88.2	53.3	9.7	67.2	45.8	8.1	65.1	39.2	3.6	64.0	40.8	3.3	64.0	44.1	De Palma et al., GCN 9867
090902462	GRB 090902B	11:05:08.32	262.6	29.7	4.8	266.4	33.9	3.5	261.4	26.0	1.0	261.4	26.1	1.0	264.9	27.3	Sakamoto et al., GCN 9890
090904058	GRB 090904B	01:24:13.94	257.4	-24.1	26.4	266.8	-17.9	10.1	266.6	-27.5	4.1	265.9	-30.1	1.9	264.2	-25.2	Ukwattia et al., GCN 9909
090912660	GRB 090912A	15:50:29.11	236.2	27.5	20.0	212.7	32.3	25.6	212.8	41.8	18.4	178.5	66.0	5.1	188.0	61.5	Cummings et al., GCN 9912
090915650	GRB 090915A	15:35:35.66	237.7	33.1	15.4	237.7	33.1	15.4	250.1	23.8	6.5	243.7	9.9	3.7	238.0	15.5	Uehara et al., GCN 9934
090926181	GRB 090926B	04:20:26.99	1.3	-66.1	6.2	350.0	-63.3	3.5	354.4	-64.3	1.0	350.1	-63.5	1.0	353.4	-66.3	Grupe et al., GCN 9935
090926914	GRB 090926B	21:55:28.53	38.2	-31.0	30.7	26.2	-31.7	9.5	28.2	-32.5	3.5	44.3	-43.9	2.4	46.3	-39.0	Grupe et al., GCN 9945
090927422	GRB 090927A	10:07:17.22	61.7	-68.2	18.7	61.7	-68.2	18.7	60.5	-65.9	12.3	67.6	-67.6	12.1	344.0	-71.0	McEnery et al., GCN 9985
091003191	GRB 091003A	04:35:45.59	253.1	39.6	5.1	247.7	38.2	3.7	251.6	37.3	1.0	251.2	37.3	1.0	251.5	36.6	Domarumma et al., GCN 10004
091010113	GRB 091010A	02:43:09.33	299.9	-21.2	3.6	300.0	-21.3	3.5	291.1	-23.9	1.1	293.4	-23.8	1.2	298.7	-22.5	Palmer et al., GCN 10051
091020900	GRB 091020A	21:36:43.82	138.1	67.2	14.8	149.6	75.7	5.8	172.3	63.7	3.4	174.4	52.7	3.1	175.7	51.0	Sakamoto et al., GCN 10072
091024372	GRB 091024A	08:55:58.48	337.8	27.9	25.0	78.8	46.0	8.3	356.9	56.7	10.2	340.5	55.1	2.0	339.2	56.9	Ukwattia et al., GCN 10089
091024380	GRB 091024A	09:06:29.36	338.8	55.5	19.8	28.7	70.5	14.6	346.7	53.8	3.4	336.4	55.9	1.0	339.2	56.9	de Palma et al., GCN 10163
091026550	GRB 091026A	13:11:33.02	34.8	-83.7	17.7	34.8	-83.7	17.7	26.3	-84.7	6.3	116.3	-88.3	7.4	276.6	-86.1	Baumgartner et al., GCN 10121
091031500	GRB 091031A	12:00:28.85	71.2	-56.2	10.7	76.3	-63.3	5.6	69.7	-57.6	1.6	70.5	-59.0	1.1	71.7	-57.5	Palmer et al., GCN 10165
091102607	GRB 091102A	14:34:38.37	349.9	-68.7	16.8	49.7	-63.8	15.0	62.7	-68.3	5.5	67.0	-73.4	1.5	72.6	-72.5	Nakajima et al., GCN 10188
091112737	GRB 091112A	17:41:15.83	249.7	-42.5	21.1	252.7	-47.8	10.0	258.3	-41.3	6.5	258.3	-36.7	3.2	257.7	-36.7	Stamatikos et al., GCN 10197
091120191	GRB 091120A	04:34:40.23	225.1	-19.9	11.4	225.1	-19.9	11.4	224.3	-26.9	2.9	225.4	-26.1	1.2	226.8	-21.8	Baumgartner et al., GCN 10265
091127976	GRB 091127A	23:25:45.49	41.4	-27.6	3.8	36.8	-32.2	4.6	36.0	-21.9	1.2	38.1	-21.0	1.1	36.6	-19.0	Cummings et al., GCN 10291
091208410	GRB 091208B	09:49:57.96	28.6	24.9	8.7	28.5	25.2	4.7	29.3	14.2	2.7	30.1	13.5	2.6	26.4	16.9	Krimm et al., GCN 10322
091221870	GRB 091221A	20:52:57.22	39.1	26.6	30.6	39.8	20.6	7.4	60.8	20.4	2.1	54.5	27.3	1.2	55.8	23.2	
100111176	GRB 100111A	04:12:49.70	239.7	12.3	12.3	239.7	12.3	12.3	239.9	12.0	4.3	246.0	16.0	3.9	247.	15.5	

Burst Name	Common Name	Trigger Time (UT)	FSW _{first} for Ref.		FSW _{last} for Ref.		Ground Auto for Ref.		H.i.t.L for Ref.		Ref. Location		Reference				
			(RA Dec)	(Err)	(RA Dec)	(Err)	(RA Dec)	(Err)	(RA Dec)	(Err)	(RA Dec)	(RA Dec)					
100116897	GRB 100116A	21:31:00.25	300.0	12.3	13.5	300.0	12.3	13.5	307.0	26.0	3.1	308.4	22.7	1.2	305.0	14.5	McEnery et al., GCN 10333
100117879	GRB 100117A	21:06:19.67	6.1	-6.2	11.9	6.1	-6.2	11.9	9.9	8.3	3.7	11.2	9.0	5.8	11.3	13.2	Markwardt et al., GCN 10338
100206563	GRB 100206A	13:30:05.40	44.7	17.6	11.5	44.7	17.6	11.5	74.6	22.7	3.0	63.9	13.9	4.5	47.2	13.2	Sakamoto et al., GCN 10379
100212588	GRB 100212A	14:07:22.30	7.3	48.7	10.6	7.3	48.7	10.6	4.7	45.5	4.8	2.9	44.8	4.3	356.4	49.5	Ukwatta et al., GCN 10404
100216422	GRB 100216A	10:07:00.19	148.9	46.4	17.0	148.9	46.4	17.0	157.7	49.0	7.6	155.5	47.4	8.7	154.3	35.5	Cummings et al., GCN 10428
100225115	GRB 100225A	02:45:31.15	310.2	-60.7	21.3	302.3	-67.9	10.4	319.8	-56.3	4.5	312.4	-54.7	3.3	310.3	-59.4	Piron et al., GCN 10450
100325275	GRB 100325A	06:36:08.03	327.2	-23.9	6.5	327.2	-23.9	6.9	329.1	-27.3	1.7	331.3	-28.1	2.0	330.2	-26.5	de Palma et al., GCN 10548
100401297	GRB 100401A	07:07:32.25	284.6	-25.8	19.0	284.6	-25.8	19.0	282.8	-26.9	9.5	290.0	-16.3	7.9	290.8	-8.3	Cummings et al., GCN 10567
100413732	GRB 100413A	17:33:31.93	237.9	-7.6	25.6	237.9	-7.6	25.6	245.9	-1.4	18.0	273.3	17.2	5.4	266.2	15.8	Stamatikos et al., GCN 10585
100414097	GRB 100414A	02:20:21.99	183.6	20.5	11.2	186.2	15.4	4.2	194.0	9.8	1.1	185.7	15.7	1.0	192.1	8.7	Page et al., GCN 10601
100427356	GRB 100427A	08:32:08.71	95.3	-4.0	10.2	95.4	-3.9	7.8	94.5	-3.5	3.4	91.0	-1.4	2.6	89.2	-3.5	Cummings et al., GCN 10699
100504806	GRB 100504A	19:20:55.54	250.4	-18.3	28.0	250.9	-33.6	20.3	246.2	-31.7	10.4	254.8	-34.7	5.1	255.6	-35.6	Palmer et al., GCN 10716
100510810	GRB 100510A	19:27:06.97	74.5	-35.8	15.6	345.1	-20.0	18.4	30.1	-28.6	20.6	347.1	-21.1	4.2	355.8	-35.6	Morii et al., GCN 10739
100522157	GRB 100522A	03:45:52.30	10.2	10.2	5.6	10.2	10.2	5.6	13.1	11.5	1.8	8.0	10.5	3.9	7.0	9.4	Barthelmy et al., GCN 10788
100625773	GRB 100625A	18:32:28.48	16.3	-50.0	4.8	16.3	-50.0	4.8	21.9	-38.1	2.6	21.9	-38.1	3.9	15.8	-39.1	Del Monte et al., GCN 10810
100701490	GRB 100701B	11:45:23.07	13.4	-35.3	4.9	19.1	-33.1	3.8	45.1	2.6	2.3	47.2	-3.5	1.1	43.1	-2.2	Golenetskii et al., GCN 10938
100704149	GRB 100704A	03:35:06.11	139.6	-23.5	11.2	152.4	-12.2	6.4	136.6	-19.7	2.2	133.2	-23.6	1.6	133.6	-24.2	Cummings et al., GCN 10932
100724029	GRB 100724A	00:42:06.00	154.4	84.5	16.2	131.6	85.0	4.4	128.8	70.9	1.2	116.8	73.5	1.0	120.0	76.7	Tanaka et al., GCN 10978
100725475	GRB 100725B	11:24:34.90	297.1	74.3	17.0	248.4	76.2	10.0	285.4	77.6	2.3	280.5	73.5	2.2	290.0	77.0	Sakamoto et al., GCN 10993
100727238	GRB 100727A	05:42:22.00	142.6	-10.1	34.6	142.6	-10.1	34.6	142.6	-8.2	12.2	154.6	-9.8	11.1	154.2	-21.4	Stamatikos et al., GCN 11001
100728095	GRB 100728A	02:17:30.62	77.1	-14.3	35.1	78.1	-23.4	8.6	91.3	-16.9	1.7	88.3	-13.7	1.0	88.8	-15.3	Ukwatta et al., GCN 11018
100728439	GRB 100728B	10:31:54.98	55.3	0.3	12.9	51.6	3.2	9.5	42.5	2.1	4.9	41.5	0.2	4.2	44.1	0.3	Barthelmy et al., GCN 11023
100802240	GRB 100802A	05:45:35.68	5.2	43.0	18.0	5.2	43.0	18.0	0.7	44.9	7.8	4.6	43.9	6.8	2.5	47.8	Baumgartner et al., GCN 11035
100814160	GRB 100814A	03:50:08.81	25.1	-1.2	12.0	19.1	-10.4	7.5	20.0	-16.4	3.4	19.8	-15.4	2.5	22.5	-18.0	Krimm et al., GCN 11094
100816026	GRB 100816A	00:37:50.95	-	-	-	90.3	-23.0	11.1	347.5	25.4	2.2	346.4	25.5	1.9	351.7	26.6	Markwardt et al., GCN 11111
100906576	GRB 100906A	13:49:27.63	129.7	53.3	4.2	30.3	51.9	5.6	27.3	57.1	1.6	28.0	55.2	1.1	28.7	55.6	Barthelmy et al., GCN 11233
100915243	GRB 100915B	05:49:39.62	84.7	22.9	25.4	84.7	22.9	25.4	86.8	18.3	16.4	86.8	18.3	12.7	85.4	25.1	Merghetti et al., GCN 11278
100924165	GRB 100924A	03:58:08.32	3.5	28.2	9.9	3.5	28.2	9.9	7.2	8.7	4.0	6.9	9.7	4.0	0.7	7.0	Barthelmy et al., GCN 11295
101008697	GRB 101008A	16:43:15.61	324.8	34.0	13.2	324.8	34.0	13.2	335.0	31.7	8.6	326.9	36.7	8.5	328.9	37.1	Barthelmy et al., GCN 11327
101011707	GRB 101011A	16:58:36.54	17.7	-78.2	9.7	17.7	-78.2	9.7	31.1	-61.7	11.3	33.4	-75.9	6.4	48.3	-66.0	Markwardt et al., GCN 11332
101023951	GRB 101023A	22:50:04.73	15.5	-67.7	22.4	354.7	-60.6	3.7	320.6	-67.3	1.0	315.5	-66.5	1.0	318.0	-65.4	Stamatikos et al., GCN 11367
101024486	GRB 101024A	11:39:33.61	157.5	-70.9	19.2	157.5	-70.9	19.2	144.5	-84.0	6.5	147.1	-77.2	9.6	166.4	-77.3	Ukwatta et al., GCN 11374
101030664	GRB 101030A	15:56:30.72	177.1	-35.3	31.3	177.1	-35.3	31.3	166.9	-23.1	21.7	169.5	-16.0	7.4	166.4	-16.4	Barthelmy et al., GCN 11388
101112924	GRB 101112A	22:10:32.45	299.7	42.8	8.2	299.7	42.8	8.2	300.5	39.8	3.5	299.3	39.4	4.2	292.2	39.3	Gotz et al., GCN 11396
101201418	GRB 101201A	10:01:49.75	1.6	-2.4	14.4	358.2	-6.2	7.2	0.3	-15.3	2.7	3.9	-14.7	1.6	1.9	-16.1	Cummings et al., GCN 11429
101213451	GRB 101213A	10:49:20.80	246.9	10.9	19.6	237.7	19.3	11.1	238.7	16.8	6.1	247.3	21.2	3.6	241.3	21.9	Cummings et al., GCN 11453
101219686	GRB 101219B	16:28:13.13	9.3	-39.2	23.8	9.3	-39.2	23.8	17.2	-31.0	8.4	11.1	-31.1	3.4	12.3	-34.6	Cummings et al., GCN 11475
101224227	GRB 101224A	05:27:13.87	303.9	1.6	21.6	303.9	1.6	21.6	306.8	27.2	18.7	300.3	40.4	13.5	285.9	45.7	Markwardt et al., GCN 11486
110102788	GRB 110102A	18:54:36.01	249.3	-3.5	10.1	249.2	-3.7	5.6	245.2	5.5	1.7	246.2	6.0	2.0	245.9	7.6	Sakamoto et al., GCN 11511
110106893	GRB 110106B	21:26:16.08	197.9	31.8	27.3	197.9	31.8	27.3	171.3	37.7	10.0	155.3	38.6	9.3	134.2	47.0	Ukwatta et al., GCN 11533

Burst Name	Common Name	Trigger Time (UT)	FSW _{first} for Ref.		FSW _{last} for Ref.		Ground Auto for Ref.		H.i.t.L. for Ref.		Ref. Location		Reference				
			(RA Dec)	(Err)	(RA Dec)	(Err)	(RA Dec)	(Dec)	(RA Dec)	(RA Dec)	(RA Dec)	(RA Dec)					
110112934	GRB 110112B	22:24:55.30	21.6	44.5	9.7	21.6	44.5	9.7	25.8	42.8	5.8	44.0	4.7	10.6	64.4	Mereghetti et al., GCN 11562	
110119931	GRB 110119A	15:59:39.23	65.1	-22.6	5.3	65.6	-23.0	4.9	349.6	6.0	4.4	345.4	8.0	348.6	6.0	Baumgartner et al., GCN 11584	
110128073	GRB 110128A	01:44:36.44	207.5	7.3	27.5	207.5	7.3	27.5	202.7	22.3	14.0	204.4	19.7	193.9	28.1	Omodet et al., GCN 11597	
110201399	GRB 110201A	09:35:10.26	177.3	59.8	11.3	177.3	59.8	11.3	164.8	84.4	6.5	166.3	87.4	137.6	88.6	Cummings et al., GCN 11614	
110207470	GRB 110207A	11:17:20.29	14.3	-12.3	13.4	14.3	-12.3	13.4	359.5	4.7	13.4	15.7	-10.0	5.5	12.5	-10.8	Krimm et al., GCN 11624
110213220	GRB 110213A	05:17:11.28	46.0	49.3	28.9	39.2	39.3	7.2	49.2	52.5	2.6	49.0	52.8	2.3	43.0	49.3	Palmer et al., GCN 11664
110318552	GRB 110318A	13:14:16.71	327.6	-35.1	30.0	343.7	-27.8	5.9	336.3	-16.4	2.6	335.9	-14.9	1.9	338.3	-15.3	Barthelmy et al., GCN 11714
110402009	GRB 110402A	00:12:58.55	189.0	65.0	19.8	182.1	54.5	4.5	190.2	57.2	4.1	187.7	58.7	2.2	197.4	61.3	Stamatikos et al., GCN 11866
110412315	GRB 110412A	07:33:35.71	110.5	21.3	28.4	130.4	14.4	14.6	114.6	16.6	7.9	135.9	11.4	3.8	133.5	13.5	Baumgartner et al., GCN 11929
110420946	GRB 110420B	22:42:11.74	311.3	-44.9	16.6	311.3	-44.9	16.6	350.0	-28.8	26.7	326.4	-39.3	12.2	320.1	-41.3	Markwardt et al., GCN 11946
110428388	GRB 110428A	09:18:30.41	-	-	-	128.9	12.8	6.1	0.5	62.4	1.0	2.1	61.7	1.0	5.3	64.8	Vasileiou et al., GCN 11982
110610640	GRB 110610A	15:21:32.55	313.8	76.6	17.4	317.2	78.9	6.4	310.0	77.6	2.3	306.5	75.9	2.6	308.2	74.8	Marshall et al., GCN 12065
110625881	GRB 110625A	21:08:18.24	298.0	6.7	14.1	348.4	54.6	3.4	287.8	6.9	1.0	287.7	6.7	1.0	286.8	6.8	Page et al., GCN 12088
110709642	GRB 110709A	15:24:27.37	239.9	44.6	5.4	239.9	44.6	5.2	240.4	39.9	1.5	241.2	41.8	1.1	238.9	40.9	Holland et al., GCN 12118
110721200	GRB 110721A	04:47:43.77	327.6	-37.9	3.9	323.6	-33.4	3.8	331.4	-36.6	1.0	331.4	-36.6	1.0	333.4	-39.0	Vasileiou et al., GCN 12188
110731465	GRB 110731A	11:09:29.96	281.8	-38.9	4.3	282.0	-39.0	4.4	281.1	-26.6	3.4	283.1	-34.0	1.0	280.5	-28.5	Oates et al., GCN 12215
110818860	GRB 110818A	20:37:54.23	140.4	-73.3	28.4	140.4	-73.3	28.4	338.4	-55.7	10.0	329.6	-54.1	4.1	317.4	-64.0	Markwardt et al., GCN 12279
110825102	GRB 110825A	02:26:50.94	42.4	6.5	26.9	48.8	17.3	3.7	47.1	14.6	1.0	47.1	14.6	1.0	44.8	15.4	Zhang et al., GCN 12308
110903111	GRB 110903A	02:39:34.43	195.7	63.3	8.8	208.1	65.5	6.5	199.1	52.7	3.8	196.0	51.8	2.6	197.1	59.0	Mereghetti et al., GCN 12322
110921577	GRB 110921A	13:51:22.58	296.6	47.9	18.5	296.6	47.9	18.5	297.1	41.9	6.2	297.9	33.7	3.9	294.1	36.4	Baumgartner et al., GCN 12373
111103441	GRB 111103A	10:35:13.40	330.7	-3.6	9.1	330.7	-3.6	9.1	331.2	-9.7	4.1	327.0	-10.0	1.8	327.1	-10.5	Stroh et al., GCN 12378
111107035	GRB 111107A	00:50:25.49	152.3	-63.3	17.9	152.3	-63.3	17.9	141.6	-65.3	5.7	149.0	-66.0	6.0	129.5	-66.5	Siegel et al., GCN 12554
111117510	GRB 111117A	12:13:42.03	13.2	26.8	4.8	13.2	26.8	4.8	14.4	24.0	3.1	13.8	26.0	3.1	12.7	23.0	Mangano et al., GCN 12559
111222619	GRB 111222A	14:51:55.03	207.6	59.1	3.4	207.6	59.1	3.4	189.6	65.8	3.1	173.4	65.2	1.7	179.2	69.0	Hurley et al., GCN 12714
111228657	GRB 111228A	15:45:30.81	148.5	22.2	6.7	148.5	22.2	6.7	147.3	15.2	2.4	146.6	14.6	2.4	150.1	18.3	Guver, GCN 12741
120102095	GRB 120102A	02:16:23.24	281.8	19.6	12.4	286.4	16.5	5.2	272.6	17.4	5.3	277.1	20.4	2.0	276.2	24.7	Marshall et al., GCN 12794
120114681	GRB 120114A	16:20:05.68	307.7	58.3	14.3	307.7	58.3	14.3	311.7	49.6	7.9	311.0	52.1	5.4	317.9	57.0	Sakamoto et al., GCN 12833
120118709	GRB 120118B	17:00:22.95	115.3	-24.9	29.4	115.3	-24.9	29.4	128.6	-13.9	13.3	131.2	-9.6	8.2	124.9	-7.2	Littlejohns et al., GCN 12852
120119170	GRB 120119A	04:04:25.07	113.6	-4.9	5.9	113.5	-4.8	4.5	119.2	-7.0	1.3	119.0	-9.0	1.1	120.0	-9.1	Beardmore et al., GCN 859
120212383	GRB 120212A	09:11:23.50	40.8	-13.2	21.8	40.8	-13.2	21.8	26.9	-22.5	10.3	32.9	-15.1	10.0	43.1	-18.0	Sonbas et al., GCN 12930
120302080	GRB 120302A	01:55:34.01	146.8	31.1	26.1	146.8	31.1	26.1	148.3	22.4	18.0	147.0	25.2	7.7	122.5	29.7	Sakamoto et al., GCN 13000
120312671	GRB 120312A	16:06:29.67	261.9	-6.4	18.8	261.9	-6.4	18.8	259.4	-2.3	8.7	254.3	11.5	7.8	251.8	23.9	Stamatikos et al., GCN 13049
120323507	GRB 120323A	12:10:19.73	335.3	35.6	3.3	335.3	35.6	3.3	345.8	26.5	1.0	345.8	26.5	1.0	340.4	29.7	Golenetskii et al., GCN 13102
120326056	GRB 120326A	01:20:31.52	255.8	68.0	11.9	243.6	70.7	8.8	274.1	64.8	5.3	262.2	62.1	4.2	273.9	69.3	Siegel et al., GCN 13105
120403857	GRB 120403B	20:33:58.50	291.5	-82.9	21.3	291.5	-82.9	21.3	268.8	-76.9	11.2	241.5	-80.4	12.3	55.3	-89.0	Goad et al., GCN 13205
120512112	GRB 120512A	02:41:44.34	324.4	17.1	14.0	327.5	11.8	6.6	326.3	13.3	1.2	324.7	14.7	1.8	325.6	13.6	Mereghetti et al., GCN 13300
120521380	GRB 120521B	09:07:52.39	167.1	-45.7	21.0	166.0	-48.2	25.9	192.7	-38.8	10.9	208.1	-47.1	5.2	197.0	-52.7	Cummings et al., GCN 13305
120624309	GRB 120624A	07:24:25.34	314.0	60.3	3.3	314.0	60.3	3.3	0.7	-6.3	1.2	0.7	-6.3	1.2	4.8	7.2	Sakamoto et al., GCN 13376
120624933	GRB 120624B	22:23:54.94	178.2	47.1	22.0	174.3	22.5	4.2	171.9	5.7	1.2	171.8	5.6	1.0	170.9	8.9	Sakamoto et al., GCN 13384
120703726	GRB 120703A	17:25:17.04	325.3	-32.6	17.6	345.2	-27.8	4.4	340.2	-29.1	1.6	339.8	-29.5	1.7	339.4	-29.7	Stamatikos et al., GCN 13414
120709883	GRB 120709A	21:11:40.37	338.5	-57.8	6.0	319.8	-68.0	5.0	327.0	-52.2	1.1	319.9	-50.0	1.6	318.4	-50.0	Kocevski et al., GCN 13423
120711115	GRB 120711A	02:44:53.30	69.6	-62.9	8.5	56.5	-63.7	5.7	77.2	-66.3	1.0	79.4	-66.6	1.0	94.7	-71.0	Gotz et al., GCN 13434

Burst Name	Common Name	Trigger Time (UT)	FSW _{first} for Ref. (RA Dec Err)	FSW _{last} for Ref. (RA Dec Err)	Ground Auto for Ref. (RA Dec Err)	H.i.t.L for Ref. (RA Dec Err)	Ref. Location (RA Dec)	Reference
120712571	GRB 120712A	13:42:25.61	175.4 -23.2	165.7 -28.0	8.6 172.0	175.2 -19.8	169.6 -50.1	Barthelmy et al., GCN 13455
120728934	GRB 120728A	22:25:12.74	167.1 -45.7	167.1 -45.7	21.0 131.5	138.2 -54.0	137.1 -54.4	Cummings et al., GCN 13525
120729456	GRB 120729A	10:56:12.67	-	16.5 10.8	17.5 60.2	17.0 49.2	13.1 49.9	Ukwatta et al., GCN 13530
120811649	GRB 120811C	15:34:55.09	215.3 56.6	215.3 56.4	17.2 225.9	214.4 55.8	199.7 62.3	Barlow et al., GCN 13622
120817168	GRB 120817B	04:02:29.72	-	233.5 -38.2	3.3 12.5	12.3 -23.8	3.9 8.3	Golenetskii et al., GCN 13670
120907017	GRB 120907A	00:24:24.51	80.9 0.6	80.9 0.6	14.6 77.3	74.1 -8.5	74.7 -9.3	Racusin et al., GCN 13716
120908398	GRB 120908A	22:31:00.02	238.5 -26.3	231.6 -28.7	26.5 239.4	233.3 -21.1	230.6 -25.8	Morri et al., GCN 13731
120909070	GRB 120909A	01:41:22.40	281.1 -51.3	284.7 -56.5	11.7 275.2	280.0 -59.4	275.7 -59.4	Osborne et al., GCN 13732
120911298	GRB 120911A	07:08:33.99	336.9 61.6	336.9 61.6	19.7 355.1	351.8 61.5	358.0 63.1	Cannizzo et al., GCN 13744
120913846	GRB 120913B	20:18:22.89	140.0 21.0	33.6 140.0	21.0 33.6	142.0 20.7	11.8 146.4	Helder et al., GCN 13762
120913997	GRB 120913B	23:55:58.77	234.7 -7.0	19.8 218.9	24.6 13.5	215.4 -14.2	4.4 213.6	Helder et al., GCN 13763
120916173	GRB 120916A	04:08:40.75	201.7 34.3	201.7 34.3	13.4 196.0	209.7 39.6	1.7 205.8	Vianello et al., GCN 13777
120922939	GRB 120922A	22:32:09.47	308.3 -41.7	21.0 308.3	-41.7 21.0	231.1 -23.9	7.1 234.8	Yershov et al., GCN 13793
121011469	GRB 121011A	11:15:25.70	215.5 73.1	25.8 277.3	45.9 11.4	261.2 44.2	5.7 260.2	Racusin et al., GCN 13845
121031949	GRB 121031A	22:47:15.27	184.0 -6.8	26.2 176.4	6.3 11.7	162.9 -10.3	5.7 173.1	D'Elia et al., GCN 13934
121123421	GRB 121123A	10:06:00.59	316.9 -27.7	25.0 307.3	-8.9 8.8	306.7 -14.0	5.2 307.8	Helder et al., GCN 13982
121125356	GRB 121125A	08:32:29.63	203.7 43.0	19.6 209.9	53.4 13.2	235.7 57.1	3.4 229.1	Barlow et al., GCN 13993
121128212	GRB 121128A	05:05:50.96	278.7 28.7	16.7 278.3	33.6 5.7	272.6 38.9	2.2 278.8	Oates et al., GCN 14007
121202181	GRB 121202A	04:20:09.17	257.9 30.4	34.9 257.9	30.4 34.9	249.7 41.8	11.6 246.5	Oates et al., GCN 14032
121211574	GRB 121211A	13:47:03.59	190.0 46.7	15.7 190.0	46.7 15.7	208.4 35.6	10.6 206.2	Mangano et al., GCN 14057
121217313	GRB 121217A	07:30:01.58	178.1 -75.3	17.6 157.6	-70.8 15.9	149.5 -51.5	19.6 160.1	Siegel et al., GCN 14059
130206817	GRB 130206A	19:36:30.45	149.4 -58.5	17.6 149.4	-58.5 17.6	0.9 140.4	50.5 140.4	De Pasquale et al., GCN 14089
130215063	GRB 130215A	01:31:26.02	37.7 35.9	14.3 37.7	35.9 14.3	37.6 18.7	4.7 38.5	D'Elia et al., GCN 14204
130216790	GRB 130216B	18:58:11.70	66.1 -2.2	9.4 64.0	7.7 6.8	60.4 4.0	3.0 61.7	Cummings et al., GCN 14232
130216927	GRB 130216A	22:15:21.42	68.1 16.1	8.5 64.8	20.2 7.2	69.4 16.3	1.7 69.4	Melandri et al., GCN 14223
130305486	GRB 130305A	11:39:11.37	110.0 48.1	4.2 110.6	48.0 10.0	120.1 50.1	1.0 119.7	Cummings et al., GCN 14257
130306991	GRB 130306A	23:47:25.57	279.0 -12.6	50.0 279.0	-12.6 50.0	278.0 -12.6	1.0 276.9	Barthelmy et al., GCN 14279
130310840	GRB 130310A	20:09:41.50	154.8 -21.4	26.8 127.3	1.4 3.4	158.2 -25.2	14.3 142.0	Guirrec et al., GCN 14282
130325203	GRB 130325A	04:51:54.30	133.8 -18.4	10.4 127.7	-19.5 5.6	130.9 -19.7	1.6 130.7	Vianello et al., GCN 14332
130327350	GRB 130327B	08:24:04.05	218.9 -67.2	7.2 219.4	-67.1 4.8	208.0 -74.8	2.1 207.6	Ohno et al., GCN 14347
130420313	GRB 130420A	07:30:19.92	188.0 55.2	15.9 188.0	55.2 15.9	202.4 54.7	4.7 196.1	Page et al., GCN 14406
130420539	GRB 130420B	12:56:32.99	176.4 56.5	28.9 176.4	56.5 28.9	184.1 53.0	15.0 184.8	Oates et al., GCN 14411
130427324	GRB 130427A	07:47:06.42	170.6 47.7	3.4 170.7	48.1 3.2	169.9 24.3	1.0 172.5	Maselli et al., GCN 14448
130502327	GRB 130502B	07:51:11.76	57.8 59.8	14.9 52.7	64.7 4.0	72.5 69.8	1.0 77.0	Kocevski et al., GCN 14532
130502743	GRB 130502A	17:50:30.74	130.9 14.3	12.3 130.9	14.3 12.3	134.1 7.8	8.5 133.7	Troja et al., GCN 14527
130504978	GRB 130504C	23:28:57.52	93.3 0.9	27.1 87.4	9.3 3.9	90.3 4.1	1.0 90.7	Kocevski et al., GCN 14574
130515056	GRB 130515A	01:21:17.88	296.7 -51.8	11.1 296.7	-51.8 11.1	297.7 -48.4	2.1 291.5	Malesani et al., GCN 14650
130518580	GRB 130518A	13:54:37.53	354.7 43.7	10.3 354.5	44.2 3.8	356.3 47.1	1.0 356.3	Cummings et al., GCN 14676
130528695	GRB 130528A	16:41:24.41	245.5 83.0	11.1 197.1	86.2 6.7	84.2 81.6	2.1 68.1	D'Elia et al., GCN 14711
130606497	GRB 130606B	11:55:33.63	203.2 45.9	7.3 197.0	50.0 3.5	222.3 -18.8	1.0 222.3	Vianello et al., GCN 14795
130609129	GRB 130609A	03:05:10.69	146.4 15.2	16.0 146.4	15.2 16.0	150.3 28.3	12.7 148.3	Cummings et al., GCN 14828
130609902	GRB 130609B	21:38:35.61	95.5 -67.0	10.3 105.9	-64.5 4.0	55.5 -33.0	1.8 51.9	Krimm et al., GCN 14841
130610133	GRB 130610A	03:12:10.50	217.8 29.0	23.9 223.4	27.0 11.9	216.7 28.0	5.8 226.5	Cummings et al., GCN 14842

Table 10: 134 locations for GRBs that were also triangulated by IPN. All RA, Dec, Err, and Width are in units of degree. ¹These 9 bursts have 2 intersecting arcs, in which the columns are as follows: RA, Dec, box side 1, box side 2.

Burst Name	Common Name	Trigger Time			IPN Annulus			FSW _{first} for IPN			FSW _{last} for IPN			Ground Auto for IPN			H.i.t.L. for IPN			
		(UT)	(RA)	(Dec)	(RA)	(Dec)	(Err)	(Width) ¹	(RA)	(Dec)	(Err)	(RA)	(Dec)	(Err)	(RA)	(Dec)	(Err)	(RA)	(Dec)	(Err)
080715950	GRB 080715A	22:48:40.17	148.6	14.5	60.5	0.3	-	-	-	-	-	210.6	12.8	3.3	213.3	12.2	2.5	213.3	12.2	2.5
080723985	GRB 080723D	23:37:42.71	158.4	10.2	70.9	0.1	-	-	-	-	-	57.7	78.7	1.3	52.9	79.1	1.0	52.9	79.1	1.0
080724401	GRB 080724A	09:37:40.61	-	-	-	-	-	-	-	-	-	356.2	32.6	1.6	357.1	32.0	1.1	357.1	32.0	1.1
080730520	GRB 080730A	12:29:15.41	-	-	-	-	-	-	-	-	-	246.3	5.5	4.1	246.3	5.5	2.5	246.3	5.5	2.5
080730786	GRB 080730B	18:51:38.19	165.9	6.5	79.0	0.1	-	-	-	-	-	246.6	27.7	2.0	246.6	27.7	1.9	246.6	27.7	1.9
080802386	GRB 080802A	09:15:10.53	-	-	-	-	-	-	-	-	-	185.9	22.0	7.9	157.5	40.4	14.2	157.5	40.4	14.2
080803772	GRB 080803A	18:31:22.05	169.9	4.4	84.5	0.5	-	-	-	-	-	145.8	75.5	8.1	322.6	65.6	6.4	322.6	65.6	6.4
080806896	GRB 080806B	21:29:40.83	173.0	2.8	74.1	0.3	-	-	-	-	-	239.2	43.5	2.7	243.1	47.3	2.0	243.1	47.3	2.0
080807993	GRB 080807A	23:50:32.64	-	-	-	-	-	-	-	-	-	100.9	-14.2	3.6	101.6	-16.0	2.7	101.6	-16.0	2.7
080816503	GRB 080816A	12:04:18.18	181.3	-1.9	56.1	0.2	-	-	-	-	-	152.8	43.0	4.2	155.2	42.0	2.6	155.2	42.0	2.6
080816989	GRB 080816B	23:43:54.70	2.1	2.4	82.4	0.3	-	-	-	-	-	290.8	-6.0	8.5	290.7	-6.0	5.0	290.7	-6.0	5.0
080817161	GRB 080817A	03:52:10.54	182.2	-2.4	38.9	0.2	-	-	-	-	-	150.7	-17.7	2.1	149.0	-17.8	1.3	149.0	-17.8	1.3
080817720	GRB 080817B	17:17:07.52	2.3	2.6	83.6	0.2	-	-	-	-	-	80.8	-30.5	9.5	85.8	-28.0	6.9	85.8	-28.0	6.9
080821332	GRB 080821A	07:57:26.48	185.7	-4.3	73.2	0.3	-	-	-	-	-	233.8	33.2	3.0	238.5	33.5	3.9	238.5	33.5	3.9
080824909	GRB 080824A	21:48:54.73	-	-	-	-	-	-	-	-	-	122.7	-1.2	1.3	122.4	-2.7	1.3	122.4	-2.7	1.3
080825593	GRB 080825C	14:13:48.11	189.1	-6.2	45.7	0.1	-	-	-	-	-	231.0	-2.1	1.1	231.3	-3.1	1.0	231.3	-3.1	1.0
080830368	GRB 080830A	08:50:16.34	192.7	-8.2	50.6	0.2	-	-	-	-	-	138.0	31.9	4.3	158.7	30.4	2.6	158.7	30.4	2.6
080906212	GRB 080906B	05:05:11.55	197.3	-10.8	13.7	0.4	-	-	-	-	-	187.7	-7.4	2.3	190.6	-8.5	2.2	190.6	-8.5	2.2
080925775	GRB 080925A	18:35:56.00	21.9	13.7	71.3	0.2	-	-	-	-	-	95.1	18.7	1.6	95.1	17.6	1.2	95.1	17.6	1.2
081003644	GRB 081003C	15:27:17.94	-	-	-	-	-	-	-	-	-	267.2	26.1	5.2	254.5	40.3	5.6	254.5	40.3	5.6
081009140	GRB 081009A	03:20:58.07	189.3	-5.2	65.9	0.5	-	-	-	-	-	252.2	14.7	3.7	250.4	20.6	1.0	250.4	20.6	1.0
081009690	GRB 081009B	16:33:37.34	8.8	4.9	58.8	0.6	-	-	-	-	-	53.0	24.8	9.2	71.5	16.4	6.8	67.5	13.6	2.8
081021398	GRB 081021A	09:33:28.02	189.7	-2.0	23.7	0.5	-	-	-	-	-	212.9	-16.3	13.8	203.6	-26.0	8.8	197.2	-28.2	4.0
081101532	GRB 081101B	12:45:24.09	202.0	-6.8	24.7	0.3	-	-	-	-	-	219.5	-29.5	10.5	220.2	-29.5	5.2	212.3	-28.0	2.3
081102365	GRB 081102B	08:45:00.51	203.3	-7.4	38.6	0.1	-	-	-	-	-	247.1	35.8	13.6	242.8	31.0	8.6	242.8	31.0	8.6
081110601	GRB 081110A	14:25:43.04	33.5	11.8	74.3	0.2	-	-	-	-	-	116.9	24.9	4.9	112.6	21.8	2.1	111.7	21.5	2.2
081122520	GRB 081122A	12:28:12.22	-	-	-	-	-	-	-	-	-	339.2	33.9	4.2	339.3	33.9	1.0	338.3	39.8	1.0
081125496	GRB 081125A	11:53:39.01	64.5	21.8	46.1	0.1	-	-	-	-	-	45.8	-24.6	6.8	41.0	-22.7	4.3	45.5	-20.1	1.1
081129161	GRB 081129A	03:52:04.27	-	-	-	-	-	-	-	-	-	58.0	-64.7	4.3	58.0	-64.7	4.3	59.8	-60.3	2.6
081207680	GRB 081207A	16:18:46.94	-	-	-	-	-	-	-	-	-	106.4	75.0	12.9	123.4	66.0	6.5	110.2	70.2	1.9
081215784	GRB 081215A	18:48:36.85	78.7	17.7	51.6	0.5	-	-	-	-	-	10.6	44.1	3.4	10.6	44.1	3.4	124.0	50.7	1.3
081215880	GRB 081215B	21:06:53.04	-	-	-	-	-	-	-	-	-	235.5	-51.2	19.0	227.8	-52.6	14.8	231.4	-49.7	6.1
081224887	GRB 081224A	21:17:55.42	-	-	-	-	-	-	-	-	-	214.2	77.3	4.2	212.5	72.2	3.9	201.7	75.2	1.0
081231140	GRB 081231A	03:21:01.94	273.1	-24.1	54.2	0.1	-	-	-	-	-	214.3	-35.4	9.3	215.2	-36.6	4.7	211.8	-37.3	1.1

Burst Name	Common Name	Trigger Time (UT)	IPN Annulus		FSW _{first} for IPN			FSW _{last} for IPN			Ground Auto for IPN			H.i.t.L. for IPN				
			(RA)	(Dec)	(RA)	(Dec)	(Err)	(RA)	(Dec)	(Err)	(RA)	(Dec)	(Err)	(RA)	(Dec)	(Err)		
090108020	GRB 090108A	00:29:02.37	268.1	-20.2	70.7	258.6	53.9	5.5	258.6	53.9	5.5	258.6	53.9	5.5	258.6	53.9	5.5	
090112729	GRB 090112B	17:30:15.46	103.5	23.7	86.5	194.1	19.3	8.4	194.1	19.3	8.4	193.8	24.9	2.1	193.3	25.9	1.2	
090131090 ¹	GRB 090131A	02:09:21.15	349.21 ¹	18.47 ¹	0.0245 ¹	33.4	28.1	29.4	353.3	16.1	3.9	352.9	20.5	1.6	352.4	20.9	1.2	
090202347	GRB 090202A	08:19:30.41	332.2	-12.3	56.9	0.4	260.3	-15.9	22.4	260.4	-15.9	7.4	280.7	-9.6	4.7	276.4	-4.8	3.3
090207777	GRB 090207A	18:39:10.84	158.7	8.7	78.3	244.5	14.7	9.8	243.5	34.9	9.8	242.3	38.0	4.2	243.5	36.9	4.2	
090227310	GRB 090227A	07:25:57.01	320.3	-16.6	46.8	9.1	-42.5	9.2	4.2	-45.9	7.3	2.5	-42.2	2.2	2.5	-42.1	1.2	
090228204 ¹	GRB 090228A	04:53:20.92	98.52 ¹	-28.61 ¹	0.1158 ¹	108.8	-36.1	3.3	108.8	-36.1	3.3	103.3	-26.7	1.6	103.3	-26.7	1.4	
090304216	GRB 090304A	05:10:48.16	332.5	-6.4	82.7	276.8	-77.9	25.3	204.5	-73.3	21.0	223.4	-71.9	9.1	244.2	-77.7	22.2	
090305052	GRB 090305B	01:14:35.73	151.6	6.7	63.5	168.5	77.5	7.0	168.5	77.5	7.0	144.6	65.9	3.3	141.5	62.4	6.8	
090308734	GRB 090308B	17:36:24.70	329.3	-8.0	62.1	22.4	-58.1	5.1	22.4	-58.1	5.1	32.3	-54.0	2.1	18.6	-55.1	3.2	
090328713	GRB 090328B	17:07:04.94	207.5	-7.8	64.6	0.5	157.4	52.8	8.2	157.4	52.8	8.2	162.7	34.0	5.3	155.5	29.2	9.7
090330279	GRB 090330A	06:42:22.10	154.3	11.1	21.9	0.6	142.0	-4.6	29.7	142.0	-4.6	29.7	159.9	-8.8	2.5	158.9	-8.4	2.6
090411838	GRB 090411A	20:06:36.89	164.7	9.1	79.1	159.9	-63.8	6.9	162.8	-64.8	6.5	152.8	-68.3	2.4	159.2	-67.2	3.9	
090411991	GRB 090411B	23:47:44.88	352.8	-4.3	53.4	9.4	-28.2	30.8	47.1	7.7	8.9	30.9	-0.8	6.9	38.8	4.9	2.4	
090413122	GRB 090413A	02:55:57.25	346.7	-8.3	77.0	-	-	-	-	-	-	253.2	-25.1	10.0	285.3	-4.1	6.5	
090425377	GRB 090425A	09:03:30.57	-	-	-	127.3	58.1	14.7	109.1	68.8	6.9	100.3	71.7	2.2	103.7	71.2	1.4	
090429753	GRB 090429D	18:03:57.52	-	-	-	128.2	13.8	8.3	128.2	13.8	8.3	124.6	6.7	8.5	124.4	7.9	4.9	
090514006	GRB 090514A	00:08:39.16	25.9	7.4	19.2	8.9	-14.3	5.8	8.7	-14.3	6.7	8.8	-12.3	5.3	8.8	-12.3	3.6	
090514726	GRB 090514B	17:26:07.34	26.7	7.6	74.7	304.3	-24.4	5.5	304.3	-24.4	5.5	304.5	-22.3	1.9	303.2	-23.1	2.6	
090516137	GRB 090516B	03:17:20.17	208.9	-8.5	85.1	122.3	-67.7	34.3	133.7	-55.5	25.9	105.2	-68.8	5.9	104.7	-70.3	2.5	
090516853	GRB 090516C	20:28:40.05	30.0	9.1	27.8	16.9	-14.4	6.5	16.9	-14.4	6.3	23.8	-18.9	3.9	24.0	-19.0	3.7	
090518244	GRB 090518B	05:51:04.67	-	-	-	210.4	-18.6	8.7	210.4	-18.6	8.7	206.7	-16.8	5.1	210.4	-15.9	4.5	
090520850	GRB 090520C	20:23:19.31	37.0	12.1	82.4	110.2	-19.4	7.0	110.5	-19.0	6.8	118.5	-17.6	2.5	117.2	-17.9	1.6	
090524346	GRB 090524A	08:17:56.24	223.2	-14.4	83.4	309.7	-64.4	10.9	319.2	-68.0	5.3	332.4	-67.5	1.9	329.2	-67.7	1.9	
090528516	GRB 090528B	12:22:31.29	51.2	17.3	90.0	301.4	39.4	14.1	313.1	33.1	4.9	311.5	31.0	1.0	312.7	30.8	1.0	
090529564	GRB 090529C	13:32:00.49	206.3	-9.7	69.3	168.0	40.8	4.4	164.2	36.8	3.9	162.0	45.5	2.1	162.4	47.4	2.1	
090530760	GRB 090530B	18:14:24.44	56.0	18.9	14.6	75.4	8.8	12.1	77.3	13.4	4.9	73.5	14.8	1.2	72.1	14.3	1.3	
090606471	GRB 090606A	11:18:08.01	251.4	-22.7	73.1	5.4	-77.4	15.5	85.4	-77.4	15.5	150.2	-71.7	8.6	135.4	-74.2	5.7	
090610648	GRB 090610A	15:33:25.94	81.6	24.4	17.4	82.6	32.9	13.5	82.6	32.9	13.5	87.7	36.1	11.0	86.6	36.6	11.7	
090612619	GRB 090612A	14:50:50.50	86.4	24.8	19.3	80.3	14.4	7.8	76.4	17.5	7.3	71.9	13.3	5.0	67.8	11.1	3.5	
090617208	GRB 090617A	04:59:58.58	97.4	25.2	12.5	86.8	53.0	11.3	86.8	53.0	11.3	79.6	26.8	7.0	79.4	22.7	7.6	
090620400 ¹	GRB 090620A	09:36:23.47	234.25 ¹	64.70 ¹	0.0338 ¹	228.6	60.9	6.9	243.1	68.0	4.6	238.6	61.8	1.4	237.4	61.2	1.1	
090623107	GRB 090623A	02:34:17.57	223.9	-15.8	77.9	312.3	-52.0	7.3	313.2	-47.6	6.6	307.3	-47.6	3.4	312.0	-44.9	1.5	
090717034	GRB 090717A	00:49:32.11	61.3	20.3	87.3	95.0	-66.3	9.2	97.2	-62.0	4.8	92.0	-63.7	3.0	87.1	-63.7	1.2	

Burst Name	Common Name	Trigger Time		IPN Annulus		Width	FSW _{first} for IPN		FSW _{last} for IPN		Ground Auto for IPN		H.i.t.L. for IPN			
		(RA)	(Dec)	(RA)	(Dec)		(RA)	(Dec)	(RA)	(Dec)	(RA)	(Dec)	(RA)	(Dec)	(RA)	(Dec)
090718762	GRB 090718B	242.5	-20.5	32.5	-43.5	16.5	267.5	173.5	173.5	271.9	1.6	273.9	-35.0	1.1		
090719063	GRB 090719A	242.7	-20.5	74.6	-41.0	4.3	0.6	-52.3	3.8	340.4	-70.0	1.0	338.1	-69.4	1.0	
090720710	GRB 090720B	274.5	-23.9	61.1	-55.4	4.5	204.5	-55.4	4.5	203.7	-57.5	1.8	224.2	-56.2	4.7	
090802235	GRB 090802A	-	-	-	-	-	84.1	30.9	5.1	84.3	34.1	3.6	84.3	34.1	4.2	
090804940	GRB 090804A	170.6	2.4	44.3	-9.4	4.3	127.2	-9.4	4.3	129.5	-11.8	1.0	128.6	-12.2	1.0	
090809978	GRB 090809B	175.0	-0.2	76.2	8.8	9.3	87.9	8.8	9.3	88.0	8.7	4.2	97.1	0.1	1.1	
090811696	GRB 090811A	355.9	1.0	85.8	22.3	10.1	278.4	22.3	10.1	278.1	19.7	7.7	285.7	30.7	8.9	
090814368	GRB 090814C	358.4	2.4	70.5	303.8	8.6	303.8	74.8	8.6	303.8	66.1	11.3	349.7	67.0	9.9	
090814950	GRB 090814D	358.8	2.7	61.5	330.0	42.2	31.7	326.4	37.9	8.6	309.0	45.7	4.0	299.6	43.1	2.7
090820027	GRB 090820A	-	-	-	84.6	47.1	23.2	86.0	17.4	3.4	89.8	25.8	1.0	90.0	26.9	1.0
090828099	GRB 090828A	185.9	-7.4	57.9	129.0	0.3	129.0	-35.3	23.8	124.5	-26.1	5.4	123.5	-25.5	3.4	
090829672	GRB 090829A	323.06 ¹	-37.46 ¹	0.0170 ¹	326.1	-47.7	23.3	323.8	-41.2	4.5	327.3	-33.1	1.1	327.2	-33.1	1.0
090829702	GRB 090829B	-	-	-	7.1	-15.7	21.9	354.1	-17.5	9.3	351.6	-11.8	4.9	354.7	-4.3	2.4
090831317	GRB 090831A	-	-	-	87.8	55.9	9.7	87.8	55.9	9.7	148.0	50.2	6.3	145.3	49.5	2.2
090907808	GRB 090907B	-	-	-	88.8	16.3	6.1	88.8	16.3	6.1	80.7	16.5	5.2	84.3	23.2	4.8
090908341	GRB 090908B	185.8	-8.1	31.0	163.1	-12.8	30.3	165.0	-23.8	21.9	168.3	-26.6	9.2	161.8	-22.1	6.5
090910812	GRB 090910A	4.9	7.7	74.8	23.7	56.4	9.8	7.3	53.9	7.9	284.1	67.3	2.9	284.9	70.6	1.1
090922539	GRB 090922A	355.2	0.7	75.1	354.3	75.5	4.5	354.2	75.6	4.9	17.1	74.2	1.2	17.1	74.4	1.0
090922605	GRB 090922B	355.1	0.7	55.6	22.9	-22.8	21.0	52.4	-75.7	6.5	33.5	-35.5	8.7	16.4	-24.4	5.3
090925389	GRB 090925A	-	-	-	315.7	24.6	11.7	313.7	19.9	8.6	326.2	16.8	3.6	334.0	13.6	3.9
090928646	GRB 090928A	172.2	3.0	78.5	98.2	-54.2	10.2	98.1	-59.4	9.4	92.7	-53.8	9.9	94.4	-53.6	8.2
091011443	GRB 091011A	41.4	15.7	68.7	239.4	58.0	4.4	239.4	58.0	4.4	131.3	87.4	1.5	131.5	87.4	1.4
091012783	GRB 091012A	124.6	21.0	75.3	176.3	28.4	5.7	173.4	2.2	6.6	190.3	0.2	3.3	191.3	-4.7	2.9
091020977	GRB 091020B	-	-	-	40.8	22.1	6.2	40.9	22.4	4.7	42.1	24.1	1.8	42.1	23.9	1.6
091030828	GRB 091030A	-	-	-	31.6	-26.8	9.5	26.8	-35.2	6.0	24.7	-33.8	4.1	30.2	-33.4	3.3
091101143	GRB 091101A	56.2	16.4	55.9	305.0	10.0	15.8	305.4	9.9	9.8	298.3	1.9	4.2	297.0	3.4	3.3
0911227294	GRB 091227A	316.9	-18.6	83.3	225.1	-19.9	11.4	225.1	-19.9	11.4	224.3	-26.9	2.9	224.3	-26.9	1.3
091126333	GRB 091126A	65.9	16.0	41.7	53.6	-80.0	5.9	53.6	-80.0	5.9	82.7	-16.1	4.8	82.1	-17.0	4.9
091128285	GRB 091128A	-	-	-	135.9	-11.9	18.0	131.3	-3.0	5.1	128.1	4.4	1.4	128.1	1.9	1.4
091227294	GRB 091227A	294.5	-23.9	23.7	305.0	10.0	15.8	305.4	9.9	9.8	298.3	1.9	4.2	297.0	3.4	3.3
091231206	GRB 091231A	300.2	-22.7	80.4	196.3	-64.1	15.0	187.5	-54.3	8.0	196.9	-57.9	2.6	195.6	-54.0	2.1
100101988	GRB 100101B	142.2	18.9	46.7	65.2	17.1	19.6	65.2	17.1	19.6	83.0	9.2	12.9	81.8	19.5	23.7
100118100	GRB 100118A	313.8	-15.7	57.4	71.5	-81.3	14.4	71.4	-81.3	11.4	359.6	-60.6	13.3	359.2	-63.7	3.0
100122616	GRB 100122A	135.9	21.5	65.8	49.0	0.2	20.7	76.7	-11.0	4.2	88.7	-6.8	2.1	78.5	-2.1	1.6
100130777	GRB 100130B	-	-	-	144.7	31.2	16.0	69.0	25.1	17.8	78.0	19.0	5.6	79.7	23.2	2.5

Burst Name	Common Name	Trigger Time		IPN Annulus		FSW _{first} for IPN			FSW _{last} for IPN			Ground Auto for IPN			H.i.t.L. for IPN			
		(RA)	(Dec)	Err	Width	(RA)	(Dec)	Err	(RA)	(Dec)	Err	(RA)	(Dec)	Err	(RA)	(Dec)	Err	
100131730	GRB 100131A	132.4	22.5	16.4	0.3	117.0	26.2	3.9	117.0	26.2	3.9	131.2	24.8	1.3	117.5	13.8	1.5	
100205490	GRB 100205B	115.9	18.2	41.0	0.6	126.6	-33.4	21.3	134.7	-20.0	19.2	133.3	-21.4	8.6	132.6	-22.2	7.1	
100211440	GRB 100211A	-	-	-	-	120.9	31.8	5.4	120.9	31.8	5.4	138.4	30.2	3.8	133.3	29.0	2.3	
100212550	GRB 100212B	117.1	19.3	21.6	0.3	138.7	33.9	7.3	131.4	34.1	6.6	136.0	33.8	2.0	134.3	32.3	1.9	
100223110	GRB 100223A	125.4	23.8	25.0	0.1	105.9	-7.5	5.3	105.9	-7.5	5.3	94.2	3.0	6.0	102.1	5.6	7.7	
100224112	GRB 100224B	306.0	-19.3	38.2	0.2	269.8	-28.6	15.3	266.2	-9.5	6.2	271.2	-20.8	1.9	270.0	-18.7	2.2	
100225580	GRB 100225C	13.55	31.35	307.5	0.3	312.8	-0.5	19.0	312.8	-0.5	4.8	317.0	6.3	4.1	311.7	3.4	1.2	
100225703	GRB 100225D	127.9	19.2	26.1	0.3	94.5	-61.6	9.3	137.2	43.9	12.1	142.0	26.6	5.4	153.2	30.9	7.5	
100313288	GRB 100313A	145.7	15.9	74.4	0.2	157.0	-58.7	7.7	166.8	-58.8	6.5	173.4	-54.4	3.7	169.3	-52.4	3.0	
100322045	GRB 100322A	337.1	-12.2	45.7	0.1	24.7	-10.2	6.8	28.7	-5.8	4.4	22.1	-12.0	1.0	21.0	-13.4	1.0	
100324172	GRB 100324B	39.67	-19.29	0.0253	0.0431	326.0	-37.1	3.6	61.3	-12.2	4.1	25.5	-16.7	1.2	44.7	-17.3	1.0	
100326402	GRB 100326B	343.3	-9.9	28.2	0.3	303.0	12.1	23.3	308.3	13.3	18.8	312.8	-16.5	9.0	310.8	-4.6	2.1	
100330309	GRB 100330A	168.8	7.8	32.8	0.2	213.8	-1.5	11.6	208.3	-0.7	7.5	195.4	-0.1	3.2	202.8	1.8	2.9	
100410740	GRB 100410B	351.92	62.90	0.0810	0.1473	293.9	25.6	25.5	319.3	37.4	11.8	4.0	61.8	2.9	3.1	60.8	1.6	-
100421917	GRB 100421A	24.8	9.1	49.6	0.4	324.6	18.0	23.2	345.4	-19.4	14.3	343.9	-19.3	4.9	344.9	-21.1	3.2	
100423244	GRB 100423B	27.3	10.3	89.4	0.1	120.6	5.2	31.9	120.9	0.0	7.9	120.6	4.5	2.6	119.7	5.8	1.6	
100424876	GRB 100424C	30.5	11.7	36.9	0.2	39.5	32.8	22.4	39.5	32.8	22.4	44.9	30.8	14.7	17.6	46.5	2.5	-
100502356	GRB 100502A	45.9	18.0	76.6	0.1	133.3	16.8	23.8	129.6	19.9	7.9	125.7	27.1	2.8	127.7	23.9	1.6	
100503554	GRB 100503A	228.5	-18.8	79.2	0.1	145.7	-14.1	22.8	146.8	5.4	7.6	144.5	5.6	2.7	149.3	5.5	1.9	
100511035	GRB 100511A	64.3	23.4	51.9	0.1	107.8	-0.9	8.1	108.3	-8.1	4.7	111.5	-0.9	1.3	110.5	-3.2	1.0	
100517154	GRB 100517D	255.9	-25.2	25.0	0.2	236.9	-12.9	8.1	236.9	-12.9	8.1	242.1	-12.0	4.7	246.5	-9.2	4.1	
100519204	GRB 100519A	79.4	25.6	75.1	0.5	191.0	58.8	12.8	182.0	56.5	8.1	191.2	56.8	2.2	197.7	57.9	1.5	
100527795	GRB 100527A	272.8	-25.5	54.1	0.5	212.5	40.2	26.9	212.4	26.8	12.3	229.5	17.0	3.1	232.4	14.5	4.9	
100604287	GRB 100604A	281.0	-24.1	51.0	0.3	271.1	-79.5	14.3	240.0	-72.6	6.6	255.5	-75.5	2.7	245.5	-69.9	2.3	
100609783	GRB 100609A	153.7	12.3	57.2	0.7	100.0	33.8	28.2	95.4	36.5	13.4	89.9	42.0	5.4	98.1	36.1	1.5	
100612545	GRB 100612A	-	-	-	-	61.6	10.1	7.4	61.6	10.1	7.4	68.7	18.7	5.8	65.2	17.5	4.2	
100612726	GRB 100612B	288.2	-21.5	66.0	0.3	351.9	1.1	7.4	346.5	2.6	4.1	352.1	-3.1	1.2	352.1	-3.0	1.1	
100620119	GRB 100620A	88.99	-50.72	0.1593	0.2504	79.6	-52.6	8.4	79.7	-52.5	8.2	91.4	-51.8	3.6	93.0	-52.3	2.1	
100629801	GRB 100629A	227.62	29.55	0.0196	0.1297	212.2	33.1	4.7	212.2	33.1	4.7	221.7	27.1	6.5	222.2	30.0	2.7	
100707032	GRB 100707A	357.60	-6.96	0.1594	0.0679	52.9	-47.4	3.4	3.2	-10.6	3.6	351.3	-7.3	1.0	351.3	-7.5	1.0	
100709602	GRB 100709A	169.1	5.6	23.7	0.2	143.6	3.1	13.6	155.3	-8.1	12.0	152.5	-3.8	8.7	142.3	20.7	4.2	

C. Dependence of the single-component systematic error on GRB location in spacecraft coordinate system

Results for single-component models exploring the effects of GRB location in the different spacecraft hemispheres and quadrants are shown in Table 11. The first entry in the table repeats the values from Table 2 showing the single Gaussian fits for each localization type. The parameter values and odds ratio for the simplest single component fit can be compared with those for the models that split the GRBs according to position in spacecraft coordinates. GRBs localized with HitL 4.13 in the +Z and +Y hemispheres were found to have a lower systematic error than those in the -Z and -Y hemispheres and separating the sample into hemispheres was slightly preferred over a single component for the whole sky. GRBs in the $\pm Y$ quadrants appear to have smaller systematic errors than those in the $\pm X$ quadrants, and splitting the GRBs into quadrants is slightly preferred over the all-sky single-component model, but the odds ratio for this model was, however, still much lower than the core-plus-tail model in Table 3. which is thus greatly preferred over any of the single-component models. The odds ratio for these models was, however, still much lower than the core-plus-tail model in Table 3 .

D. Dependence of the core-plus-tail systematic error model on GRB spacecraft hemisphere

Results for core-plus-tail models that explore the effect of GRB position in different spacecraft hemispheres are shown in Table 12. The odds ratios for these hemisphere-dependent models should be compared with the simplest all-sky core-plus-tail, repeated from Table 3 as the first entry. Only HitL 4.14g showed a difference from the all-sky core-plus-tail model, with lower parameter values in the +Z hemisphere. By comparing the odds ratios for the two models, we can see that this hemisphere-dependent model is not preferred statistically, but the parameter values are different enough that with a much larger reference sample, this model may become favored over a single core-plus-tail model. HitL 4.13 showed no parameter difference for the core-plus-tail division into Z hemispheres, and the Ground-Auto localization sample failed to converge using this 6-parameter model. In general the division into hemispheres produced similar parameters with larger uncertainties; some juggling of events between the core and the tail can account for the slight differences in parameter values, with the exception of HitL 4.14g and the Z hemisphere division that appears promising when a larger sample becomes available.

Single-Component Gaussian with hemisphere dependence							
Type	Hemisphere	Number GRB		Peak °	Error °	Log ₁₀ Likelihood	Log ₁₀ Odds Factor
		Point	Annuli				
Ground-Auto	All-sky	208	100	6.62	0.29	155.2	154.3
Ground-Auto	+X	208	100	6.95	0.42		
	-X			6.25	0.41	155.5	154.0
Ground-Auto	+Y	208	100	7.02	0.44		
	-Y			6.21	0.39	155.7	154.2
Ground-Auto	+Z	208	100	6.48	0.33		
	-Z			7.10	0.64	155.4	154.0
Ground-Auto	±X	208	100	7.27	0.45		
	±Y			5.96	0.38	156.3	154.8
HitL 4.14g	All-sky	212	100	5.15	0.22	224.6	223.6
HitL 4.14g	+X	212	100	5.19	0.31		
	-X			5.06	0.32	224.6	222.9
HitL 4.14g	+Y	212	100	5.26	0.32		
	-Y			5.02	0.31	224.7	222.9
HitL 4.14g	+Z	212	100	4.98	0.24		
	-Z			5.68	0.53	225.0	223.3
HitL 4.14g	±X	212	100	5.41	0.35		
	±Y			4.93	0.29	224.9	223.2
HitL 4.13	All-sky	211	100	6.23	0.26	192.6	191.7
HitL 4.13	+X	211	100	6.04	0.35		
	-X			6.41	0.37	192.7	191.1
HitL 4.13	+Y	211	100	6.84	0.39		
	-Y			5.57	0.34	194.0	192.4
HitL 4.13	+Z	211	100	5.90	0.27		
	-Z			7.57	0.66	194.0	192.5
HitL 4.13	±X	211	100	6.74	0.39		
	±Y			5.75	0.33	193.5	191.8

Table 11: Geometry-dependent single-component fits to systematic uncertainties on GBM localizations.

Core + Tail (2 Gaussians) with hemisphere dependence											
Type	Hemisphere	Number GRB		Core ◦	Error ◦	Core %	Error %	Tail ◦	Error ◦	Log ₁₀ Likelihood	Log ₁₀ odds Factor
		Point	Annuli								
Ground-Auto	All-sky	208	100	3.72	0.34	80.4	5.3	13.7	1.7	174.1	171.8
Ground-Auto	+X	208	100	3.95	0.52	82.2	7.7	14.1	2.6		
	-X			3.55	0.44	79.3	7.4	13.4	2.5	174.1	170.6
Ground-Auto	+Y	208	100	3.80	0.44	77.7	7.1	14.5	2.3		
	-Y			3.58	0.56	82.6	9.0	12.3	2.6	174.5	171.0
Ground-Auto	The Z-hemisphere model failed to produce values for the -Z parameters										
HitL 4.14g	All-sky	212	100	3.71	0.24	90.0	3.5	14.3	2.5	241.3	238.9
HitL 4.14g	+X	212	100	3.76	0.32	90.7	4.8	13.8	3.6		
	-X			3.68	0.33	89.7	5.0	15.4	3.7	241.3	237.4
HitL 4.14g	+Y	212	100	3.89	0.33	89.3	5.2	13.9	3.6		
	-Y			3.53	0.30	90.5	4.5	14.9	3.7	241.5	237.5
HitL 4.14g	+Z	212	100	3.43	0.27	88.3	4.7	12.7	2.4		
	-Z			4.36	0.52	90.4	6.0	16.2	8.2	242.5	238.5
HitL 4.13	All-sky	211	100	3.57	0.32	79.8	5.3	12.7	1.5	213.5	211.1
HitL 4.13	+X	211	100	3.48	0.39	83.1	6.3	12.9	2.2		
	-X			3.64	0.52	75.9	8.8	12.3	2.2	213.8	210.1
HitL 4.13	+Y	211	100	3.63	0.48	77.1	7.6	13.1	2.0		
	-Y			3.50	0.42	81.9	7.8	11.8	2.4	213.8	210.1
HitL 4.13	+Z	211	100	3.40	0.37	79.6	6.4	11.4	1.5		
	-Z			3.94	0.61	76.0	9.2	15.4	3.5	214.4	210.8

Table 12: Hemisphere-dependent core-plus-tail fits to systematic uncertainties on GBM localizations

REFERENCES

- Aasi, J., et al. 2013, arXiv:1304.0670
- Abadie, J., et al. 2010, *Classical & QG*, 27, 17
- . 2012, *Astrophys. J.*, 760, 12
- Abdo, A. A., et al. 2009, *Astrophys. J. Lett.*, 706, L138
- Ackermann, M., et al. 2013, *Astrophys. J. Supp.*, 209, 11
- Atwood, W. S., et al. 2009, *Astrophys. J.*, 697, 1071
- Band, D. L., et al. 1993, *Astrophys. J.*, 413, 281
- Bissaldi, E., et al. 2009, *Exp. Astron.*, 24, 47
- Briggs, M. S., et al. 1999, *Astrophys. J. Supp.*, 503, 122
- . 2009, *AIP Conf.Proc.* 1133, ed. Meegan, Gehrels, & Kouveliotou, 40
- Bromberg, O., et al. 2013, *Astrophys. J.*, 764, 179
- Connaughton, V., et al. 2013, *EAS Publications Series*, 61, 657
- de Ugarte Postigo, A., et al. 2013, *GCN Circular* 15187
- Goldstein, A. M., et al. 2012, *Astrophys. J. Supp.*, 199, 19
- Graziani, C., & Lamb, D. Q. 1996, *AIP Conf.Proc.* 384, ed. Kouveliotou, Briggs, & Fishman, 382
- Gruber, D., et al. 2014, *Astrophys. J. Supp.*, 211, 12
- Hurley, K., et al. 2013, *Astrophys. J. Supp.*, 207, 39
- Kippen, R. M., et al. 2007, *AIP Conf.Proc.* 921, 590
- Leloudas, G., et al. 2013, *GCN Circular* 14983
- Levan, A. J., et al. 2013, *GCN Circular* 14455
- Loredo, T. J. 1990, in *Maximum Entropy and Bayesian Methods*, ed. P. F. Fougère (Kluwer Academic, Dordrecht), 81
- Meegan, C., et al. 2009, *Astrophys. J.*, 702, 791

- Paciesas, W. S., et al. 2012, *Astrophys. J. Supp.*, 199, 18
- Pal'shin, V. D., et al. 2013, *Astrophys. J. Supp.*, 207, 38
- Pandey, S., et al. 2010, *Astrophys. J.*, 714, 799
- Pendleton, G. N., et al. 1999, *Astrophys. J.*, 512, 362
- Ramírez, R. S., et al. 2013, GCN Circular 14685
- Singer, L., et al. 2013, *Astrophys. J. Lett.*, 776, 34
- Sivia, D. S. 1996, *Data Analysis: A Bayesian Tutorial* (Oxford, England: Oxford Univ. Press)
- Soderberg, A. M., et al. 2010, *Nature*, 463, 513
- von Kienlin, A., et al. 2014, *Astrophys. J. Supp.*, 211, 13